Finite Element Analysis of Nonlinear Micro-Mechanical Resonators Exhibiting Internal Resonance

Undergraduate Honors Thesis

Presented in Partial Fulfillment of the Requirements for Graduation with Distinction in the Department of Mechanical Engineering at The Ohio State University

Eric Pham

Mechanical and Aerospace Engineering

Micro/Nano Multi-Physical Dynamics Lab

The Ohio State University

2019

Advisor

Dr. Hanna Cho

Abstract

The development of micro-electromechanical systems (MEMS) has significantly advanced performance in numerous technological applications. It has allowed for better sensing, transduction, and actuation in small-scaled devices. Many MEMS applications utilize oscillating mechanical structures known as micro-resonators which can easily exhibit nonlinear behavior due to their miniature size and low damping. The nonlinearity, although complex, provides rich characteristics that can be exploited in order to enhance the performances of MEMS. One very interesting class of nonlinear characteristics is internal resonance where multiple modes are interacting simultaneously when the system is driven at one mode. This phenomenon occurs when there is intermodal energy transfer between the different oscillation modes. We aim to study internal resonance in more detail using the commercial finite element software ABAQUS to obtain better insights about this mechanism. We first designed a non-uniform fixed-fixed beam having an integer ratio between the modal frequencies. Second, we studied the possible ways to realize internal resonance using finite element simulation. Last of all, we investigated how different initial conditions and the effective parameters can affect the mechanism of intermodal energy transfer. A modal analysis was initially performed on the structure to obtain the desired mode shapes and frequencies. These specifications were then employed as initial conditions so that the structure can operate dynamically. By extracting the displacement data of the structure, the time response of the system was obtained. In order to investigate its resonance behavior, fast Fourier transform (FFT) and wavelet transform (WT) were applied to the time response to help visualize the frequency content of the system. By investigating the FFT and WT plots the levels of internal resonance were identified.

Acknowledgements

I would like to express sincere gratitude to my advisor Dr. Hanna Cho for giving me the opportunity for this undergraduate research position. Dr. Cho was my professor for System Dynamics and Vibrations during my junior year. During the first day of class she had a brief presentation about all of the open research positions for her lab group. This was when I decided to email her my interest in the MEMS position. After a few meetings with Dr. Cho it was decided that my research would be focused on finite element analysis of MEMS. I would also like to thank my instructor and Ph.D. student Keivan Asadi for teaching me important concepts relating to MEMS and helping me get acquainted with the tasks involved in this research. The guidance from both Dr. Cho and Keivan have been extremely helpful throughout the entirety of my research and I have learned a great deal from these two.

I would like to thank Prof. Carlos Castro for being a great instructor for the honors undergraduate research class. He has provided me with helpful advice and feedback for delivering effective presentations on my research. His guidance has helped significantly improve my presentation skills as both a researcher and an engineer.

Last of all, I would like to thank my family and friends for all of their support. They have always been positive influences and have helped me become a better person every day. I have experienced many hard times throughout my academic career, but they have given me the encouragement and support to overcome these obstacles.

Table of Contents

Abstract 3
Acknowledgements 4
List of Figures 6
List of Tables 7
Chapter 1: Introduction 8
1.1 Background 8
1.2 Internal Resonance 10
1.3 Finite Element Analysis 14
1.4 Fast Fourier Transform and Wavelet Transform 15
1.5 Objective 16
Chapter 2: Methodology 18
2.1 Model Description 18
2.2 Modal Analysis 20
2.3 Dynamic Analysis 23
2.3 Post Processing 24
Chapter 3: Results 25
3.1 Preprocessing Results 25
3.2 Lower Mode Excitation 27
3.3 Higher Mode Excitation 31
3.4 Dominant Excitation of Lower Mode 35
3.5 Dominant Excitation of Higher Mode 39
3.6 Combined Mode Excitation 43
3.7 Discussion of Results 47
Chapter 4: Conclusion 49
4.1 Summary 49
4.2 Future Work 49
References 51
Appendix 52

List of Figures

Figure 1: Frequency Response of Lower Mode Excitation 11
Figure 2: Frequency Response of Higher Mode Excitation 12
Figure 3: Time Response of Lower Mode Excitation 13
Figure 4: Time Response of Higher Mode Excitation 13
Figure 5: Model Dimensions 18
Figure 6: Meshing 19
Figure 7: Mode 2 Shape 20
Figure 8: Mode 3 Shape 21
Figure 9: Mode 2 XY-Data 21
Figure 10: Mode 3 XY-Data 21
Figure 11: Mode 2 Generated Equation 22
Figure 12: Mode 3 Generated Equation 22
Figure 13: Mode 2 Initial Condition 23
Figure 14: Mode 3 Initial Condition 24
Figure 15: Post Processing MATLAB Code 53

List of Tables

Table 1: Material Properties 19
Table 2: Modal Frequencies 25
Table 3: Mode Shape Equations 25
Table 4: Initial Conditions for Dynamic Analysis 26
Table 5: Time Response of Lower Mode Excitation 28
Table 6: FFT of Lower Mode Excitation 29
Table 7: WT of Lower Mode Excitation 30
Table 8: Time Response of Higher Mode Excitation 32
Table 9: FFT of Higher Mode Excitation 33
Table 10: WT of Higher Mode Excitation 34
Table 11: Time Response of Dominant Excitation of Lower Mode 36
Table 12: FFT of Dominant Excitation of Lower Mode 37
Table 13: WT of Dominant Excitation of Lower Mode 38
Table 14: Time Response of Dominant Excitation of Higher Mode 40
Table 15: FFT of Dominant Excitation of Higher Mode 41
Table 16: WT of Dominant Excitation of Higher Mode 42
Table 17: Time Response of Combined Mode Excitation 44
Table 18: FFT of Combined Mode Excitation 45
Table 19: WT of Combined Mode Excitation 46

Chapter 1: Introduction

1.1 Background

Micro-electromechanical systems (MEMS) can be defined as a combination of mechanical and electrical structures consisting of micro-scaled elements [1]. Advances in microfabrication have allowed MEMS to be effectively implemented into small-scale devices. Applications include a wide variety of sensors, transducers, and actuators. For example, MEMS have been successfully applied to medical pressure sensors used to monitor blood pressure by converting mechanical stresses into electrical voltages [2]. They are also commonly used in the automotive industry by fabricating accelerometers and electronics onto a single silicon chip [2]. MEMS are essentially responsible for translating various forms of mechanical phenomena into electrical voltages.

Often used in MEMS are oscillating mechanical structures known as micro-resonators. In such systems, their performance is highly dependent on their resonance behavior. They commonly are designed to operate in the linear regime, but their miniature size and low damping can easily cause their dynamic behavior to become nonlinear. This leads to a disproportionality between the forces sustaining their motion and the resulting vibrating amplitudes [3]. Many micro-resonators exhibit large displacement instabilities and excessive noise frequency because their dynamic response at the amplitudes required for operation become nonlinear [4]. It is evident that nonlinear behavior can negatively impact performance, but it can also introduce beneficial characteristics unattainable in a linear setting. Such characteristics include amplitude-frequency dependency [5], hysteresis [6], bifurcation [7], and multi-valued responses [8]. Although linear behavior in micro-resonators has been useful for many applications, researchers have attempted to exploit the unique features of nonlinearity in order to enhance the performances of MEMS. Due to the complexity of

nonlinearity, it is still very challenging to create a system that can exhibit these phenomena while also achieving the targeted performances.

The category of nonlinearity that we want to investigate is internal resonance. Resonators can exhibit different kinds of vibration, known as oscillation modes, which differ in their patterns of deformation and frequency [9]. Nonlinearity can couple different oscillation modes in such a way where exciting one mode through external force causes energy transfer towards other modes, thus establishing complex oscillatory patterns [3]. This occurrence helps us realize internal resonance, which can be characterized as the intermodal energy transfer of the system where one mode absorbs the amplitude and frequency fluctuations of the other [4]. This phenomenon is still not fully understood to this day, so we will utilize finite element modeling to help understand it. By performing dynamic analysis in simulation, the resulting calculations will provide detailed information about the underlying dynamics and the nonlinear mechanisms involved.

During early research of MEMS, only one vibrational mode found in resonators has been studied [10]. In more recent times, however, there has been growing interest to study multiple vibrational modes in order to improve the performance of MEMS [10], introducing us to the concept of internal resonance. Recent studies of internal resonance have provided new strategies to optimize micro/nano-scale devices by demonstrating low noise frequency performances in nonlinear systems [4]. Applications that can possibly benefit from this include frequency-shift-based detectors and mechanical energy storage resonators [4]. With this knowledge, we want to capitalize on this opportunity, so it is crucial that we thoroughly investigate internal resonance in order to effectively employ it.

1.2 Internal Resonance

In order to effectively trigger internal resonance, the system must exhibit three conditions: nonlinearity, a large enough forcing, and an integer ratio between modal frequencies. For this research, the forced response of a system experiencing quadratic nonlinearities was considered when investigating internal resonance. The equations of motion for this two-degree-of-freedom system with quadratic coupling terms [11] can be described as follows:

$$\ddot{u}_1 + \omega_1^2 u_1 = -2\mu_1 \dot{u}_1 + u_1 u_2 + F_1 \cos(\Omega t + \phi_1) \quad (1)$$

$$\ddot{u}_2 + \omega_2^2 u_2 = -2\mu_2 \dot{u}_2 + u_1^2 + F_2 \cos(\Omega t + \phi_2) \quad (2)$$

Equation (1) characterizes the lower mode dynamics and Equation (2) characterizes the higher mode dynamics. ω_1 is the lower mode frequency, ω_2 is the higher mode frequency, Ω is the excitation frequency, ϕ_1 and ϕ_2 are the initial phase angles, F_1 and F_2 are the driving forces, μ_1 and μ_2 are the damping coefficients, and t is the time. The functions corresponding to the displacement, velocity, and acceleration of the system for the lower mode are denoted by u_1, $\dot{u}_1$, and $\ddot{u}_1$, respectively. For the higher mode, these functions are denoted by u_2, $\dot{u}_2$, and $\ddot{u}_2$, respectively. In the case where internal resonance is experienced, there must be an integer ratio between the modal frequencies (i.e. $\omega_1 \approx 2\omega_2$) and the forcing levels (F_1 and F_2) must be at sufficient magnitudes. In order to drive the system to vibrate at one of its mode, the excitation frequency (Ω) must be equal or similar to one of the modal frequencies (ω_1 or ω_2). The mode that is directly driven is considered as the externally resonated mode (ERM) which transfers energy to the other coupled mode known as the internally resonated mode (IRM).

The displacement functions in Equations (1) and (2) are essentially the time response for each mode. When the two are added together ($u_1 + u_2$) the total time response of the system is

obtained. By applying fast Fourier transform on the time response we can acquire the total frequency response of the system. The figures shown below are the frequency responses of this quadratic nonlinear system where internal resonance is effectively triggered. Figure 1 shows the case when the lower frequency mode is directly excited ($F_1 \neq 0, F_2 = 0$) where the lower mode is the ERM and the higher mode is the IRM. Figure 2 shows the opposite ($F_1 = 0, F_2 \neq 0$) where the higher mode is the ERM and the lower mode is the IRM.

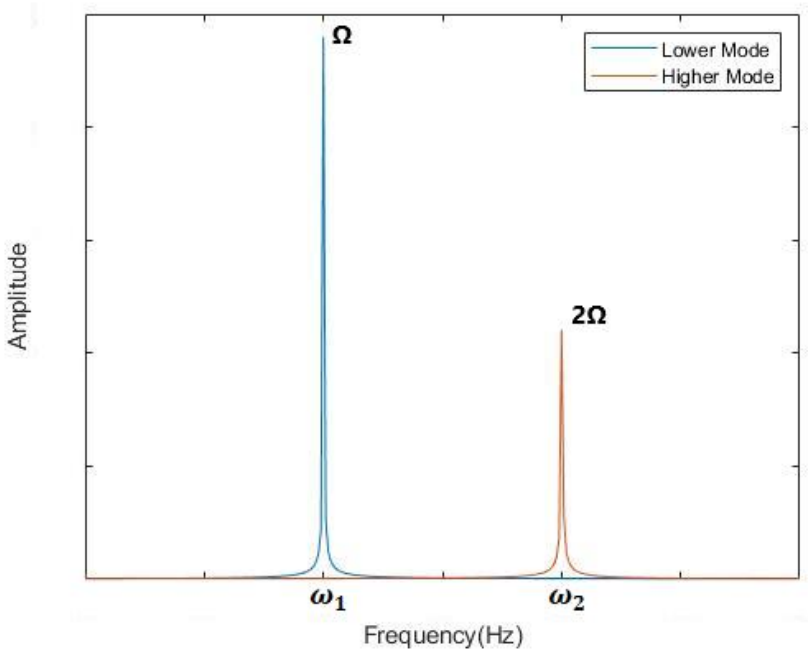

Figure 1: Frequency Response of Lower Mode Excitation

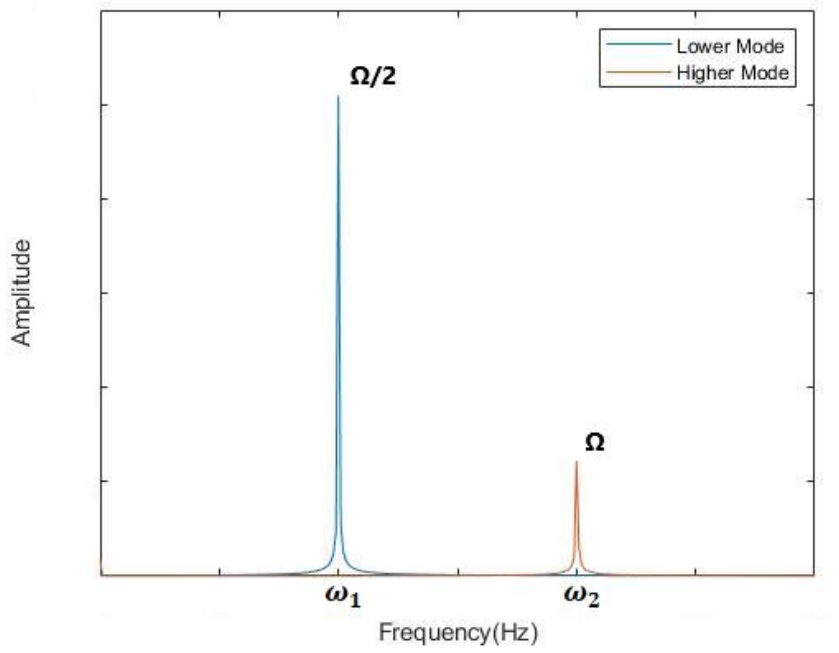

Figure 2: Frequency Response of Higher Mode Excitation

In a typical linear system, the frequency response exhibits only one peak at the drive frequency. What is unique about internal resonance is that it exhibits two peaks despite being driven at only one frequency. When all the conditions to activate internal resonance are met, the ERM can successfully transfer energy to the IRM, thus the frequency response has two resonance peaks occurring near the modal frequencies. This type of nonlinearity is specifically useful for transferring excess energy to different modes in order to stabilize the frequency of a MEMS resonator. This stabilization causes a significant decrease in frequency noise and fluctuations which many MEMS applications can benefit from.

The transfer of energy to different oscillation modes is also demonstrated in Figures 3 and 4. These results are numerically obtained when Equations (1) and (2) with $F_1 = F_2 = 0$ are numerically integrated in Matlab, when either the lower or higher mode is excited by an initial condition respectively. These show the time responses of the individual coupled modes when

internal resonance is triggered. The top subplot for each figure shows the coordinates of the lower mode (u_1) and the bottom one shows the coordinates of the higher mode (u_2). For the lower mode excitation, an initial deflection corresponding to the lower mode shape is used as the initial condition and then released to freely oscillate. For the higher mode excitation, an initial deflection at the higher mode shape is used.

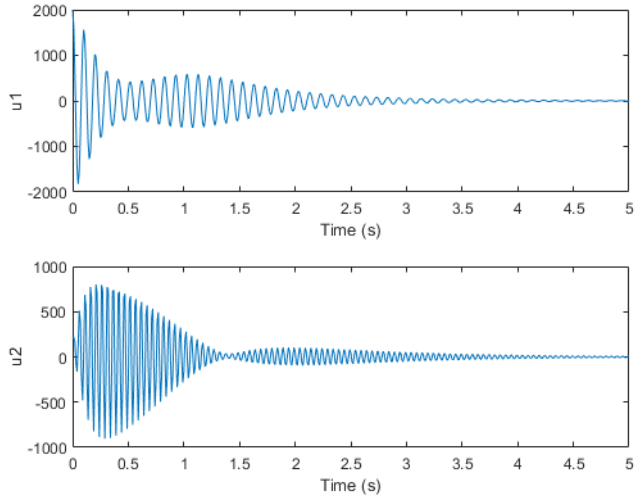

Figure 3: Time Response of Lower Mode Excitation

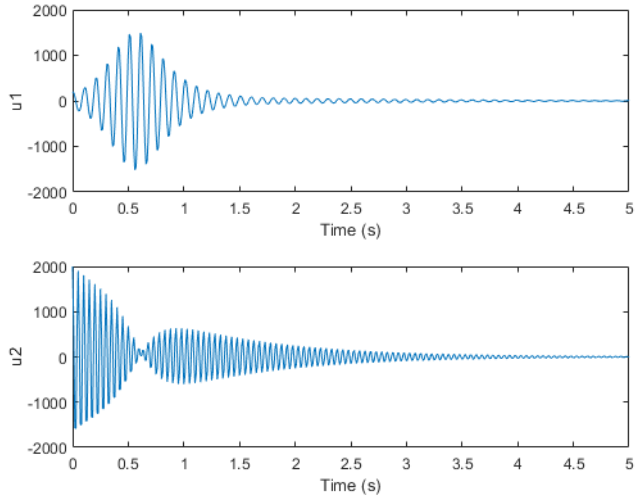

Figure 4: Time Response of Higher Mode Excitation

The time responses for the ERM initially show large displacements in amplitude which then suddenly decrease. During this process, energy is transferred from the ERM to the IRM which is why the amplitudes for the IRM suddenly increase. Once these amplitudes increase to a certain threshold, there is enough force to transfer energy back to the ERM. This occurs when the IRM amplitudes decrease while the ERM amplitudes increase. For the lower mode excitation only, energy is transferred once again from the ERM back to the IRM, but this time at a much smaller magnitude. The amplitudes of both modes eventually decay to zero which is caused by the damping. The initial conditions used for these analytical models serve as a basis for our finite element simulations.

1.3 Finite Element Analysis

Finite element analysis (FEA) is a numerical method often used in engineering applications to compute approximate solutions for complex partial differential equations. These equations are typically simplified into approximating systems of ordinary differential equations which can then be solved using standard mathematical techniques [12]. FEA initially divides the domain of a problem into multiple small subdomains known as elements. The equations that model each element are calculated individually and the results are combined to form a final solution that characterizes the entire system. FEA can accurately model complex geometries, visually spot detailed effects, and is very useful for time-dependent simulations [13], which is why it serves as an effective approach for this research.

FEA is a very practical tool for designing micro-resonators as it can accurately simulate dynamic behavior and capture nonlinear effects. It allows us to obtain data for various mechanical phenomena that typically cannot be found through other means. For this research, FEA was specifically used to examine the dynamic response of a nonlinear silicon micro-resonator. The

proposed methodology involved deflecting the structure at the corresponding mode shapes as initial conditions so that it could operate dynamically. By extracting the displacement data of the structure, we were able to obtain the time response of the system. In order to investigate its resonance behavior, the frequency content of the time response was analyzed. Assessing this data helped us identify the levels of internal resonance that the system exhibited.

1.4 Fast Fourier Transform and Wavelet Transform

Fourier transform (FT) and wavelet transform (WT) are two signal processing techniques that can effectively capture the frequency content of a system. Since these characteristics are not readily observable within the time response, the time domain signal must be transformed into the frequency domain. This is performed mathematically by representing the time domain signal as a series of coefficients [14] shown in the equation below:

$$c_n = \int_{-\infty}^{\infty} x(t)\psi_n^*(t)\,dt$$

The time domain signals are represented by $x(t)$ and the template functions are represented by $\psi_n(t)$. By taking the inner product between the time domain signals and template functions, the similarities between the two are realized [14] which is expressed as:

$$\langle x, \psi_n \rangle = \int x(t)\psi_n^*(t)dt$$

By performing FT, the time domain and a series of sine and cosine functions (used as template functions) are convoluted [14]. The FT of a signal is expressed by the equation below:

$$X(f) = \langle x, e^{i2\pi ft} \rangle = \int x(t)e^{-i2\pi ft}dt$$

This equation measures the similarity between $x(t)$ and the template sine/cosine functions and calculates the average frequency information for the entire period of the signal analyzed [14]. One fallback of FT, however, is that it does not reveal the frequency content at specific points in time.

Unlike FT, WT can display the frequency content and intensity of a system over different periods of time. WT utilizes small oscillating waves called wavelets. By comparing the time domain signal with a set of functions obtained by the scaling and shifting of a wavelet, different frequency components within a signal can be analyzed within variable windows of time [14]. The WT is defined by the equation below:

$$X(a,b) = \frac{1}{\sqrt{b}} \int_{-\infty}^{\infty} x(t)\psi\left(\frac{t-a}{b}\right) dt$$

The variable a shifts the time, b modulates the width of the window size, and $\psi(t)$ is the function of the wavelet. For this research the Morlet wavelet was used since it can identify transient components embedded in a signal [14]. The function of the Morlet wavelet is expressed as:

$$\psi(t) = \frac{1}{\sqrt{\pi f_b}} e^{i2\pi f_c t} e^{-\frac{t^2}{f_b}}$$

In order to capture the levels of internal resonance that a system exhibits, its frequency content must be analyzed. In order to effectively visualize this, Fast Fourier Transform (FFT) and discrete WT must be performed on the time response of the system.

1.5 Objective

The long-term goal of this research is to exploit the unique features of internal resonance to design a tunable nonlinear micro-resonator based on the firm understanding about its mechanism. This involved establishing a robust mechanical system having an integer ratio between

the modal frequencies (e.g. 1:2). The system consisted of a non-uniform beam that was fixed on both sides. By utilizing modal and dynamic analyses through FEA simulation, the effects of different parameters and initial conditions on internal resonance were investigated. By applying different mode shapes and frequencies to the structure, the mechanism of intermodal energy transfer was attempted to be assessed.

Chapter 2: Methodology

2.1 Model Description

The structure modeled for this research was a non-uniform silicon beam. All finite element simulations were performed using ABAQUS. Figure 5 shows the dimensions and boundary conditions for the model. Table 1 shows the material properties used. Through analytical modeling, it was found that this beam design could provide the strongest internal resonance effect by coupling the second and third modes, meaning that they exhibited the most energy transfer [15]. The beam was designed non-uniformly causing the mode shapes to be asymmetric which helps enhance the internal resonance coupling effect [15]. Standard values of density and Poisson's ratio for silicon were used. The Young's Modulus value was altered within a reasonable range until the second mode frequency was approximately half the third mode frequency in order to achieve a 1:2 ratio between the modal frequencies.

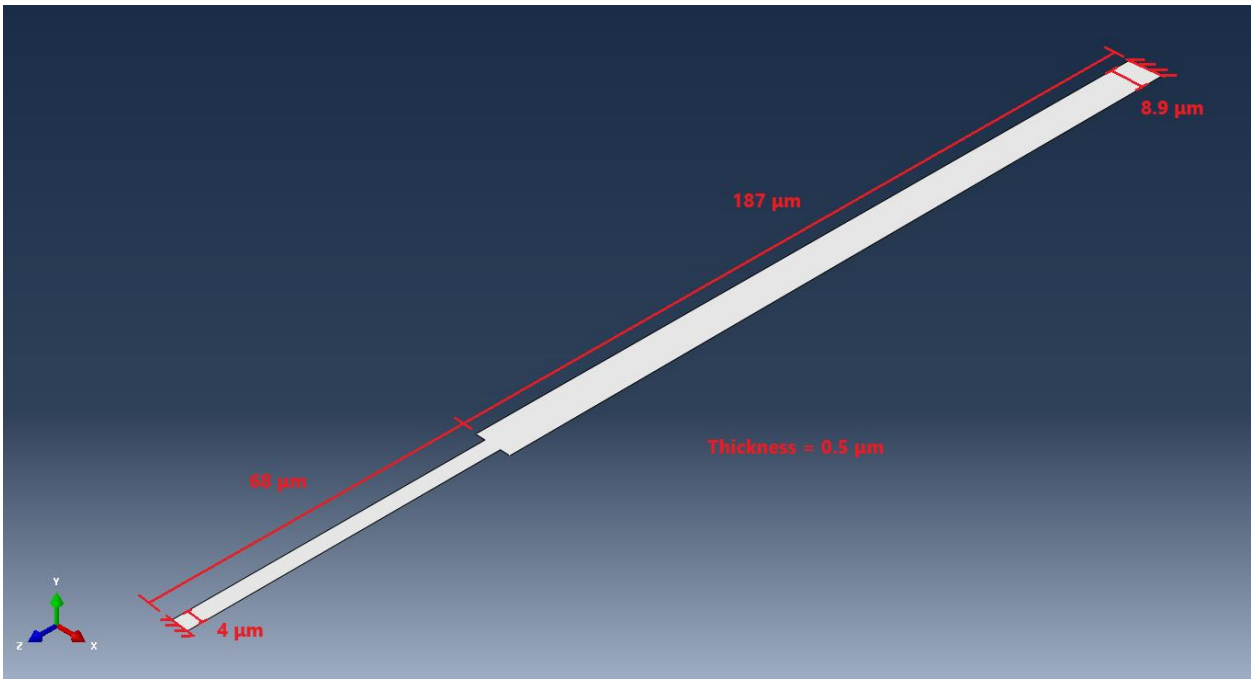

Figure 5: Model Dimensions

Table 1: Material Properties

Material	Silicon
Density	2330 kg/m^3
Young's Modulus	124 GPa
Poisson's Ratio	0.24

A simple structural mesh was applied to the beam as shown in Figure 6. The structure was modeled two-dimensionally so that shell elements could be used. One benefit to this approach is that it is very accurate at simulating structures with very small thicknesses. Solid elements were used for previous simulations which rendered significantly long calculation times. In order to obtain results in a more efficient manner, shell elements were used instead. Since this approach uses less elements, calculation times were significantly decreased. The element type was set to linear rather than quadratic in order to decrease calculation times as well. A convergence analysis was performed to ensure that the meshing provided accurate results. The final mesh generated a total of 1536 elements and 1771 nodes.

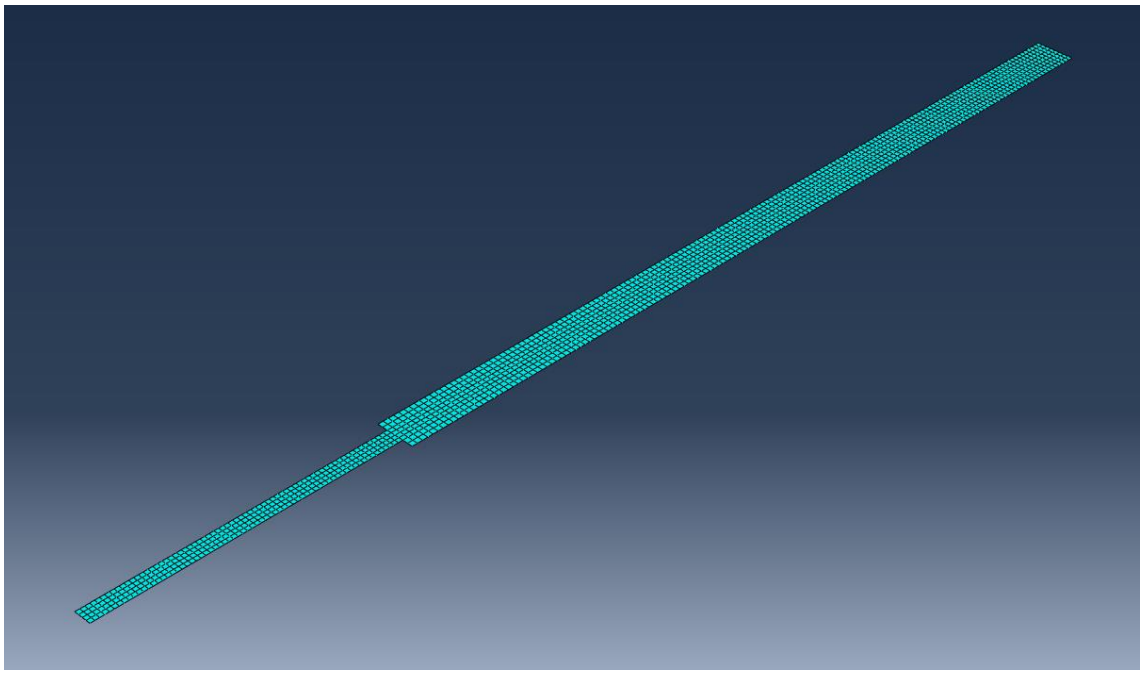

Figure 6: Meshing

2.2 Modal Analysis

Once the proper material specifications, boundary conditions, and meshing were implemented, a linear perturbation analysis was conducted to obtain the first few mode shapes of the structure and their corresponding natural frequencies. Using the first two modal frequencies, the damping coefficient was calculated using the following equation:

$$\alpha = 2\omega_1\omega_2 \frac{0.001\omega_2 - 0.001\omega_1}{\omega_2^2 - \omega_1^2}$$

The second and third mode shapes are shown in Figures 7 and 8 respectively. Internal resonance between these two modes was analyzed since they were calculated to have the strongest coupling. A path was created lengthwise along the edge of the structure which was then exported as XY-data onto Excel for both mode shapes. This data was then imported into MATLAB's curve fitting tool where equations defining these mode shapes were generated. The XY-data of these mode shapes along with their fitted curves are shown in Figures 9 and 10. The sum of sines equations characterizing the fitted data are shown in Figures 11 and 12.

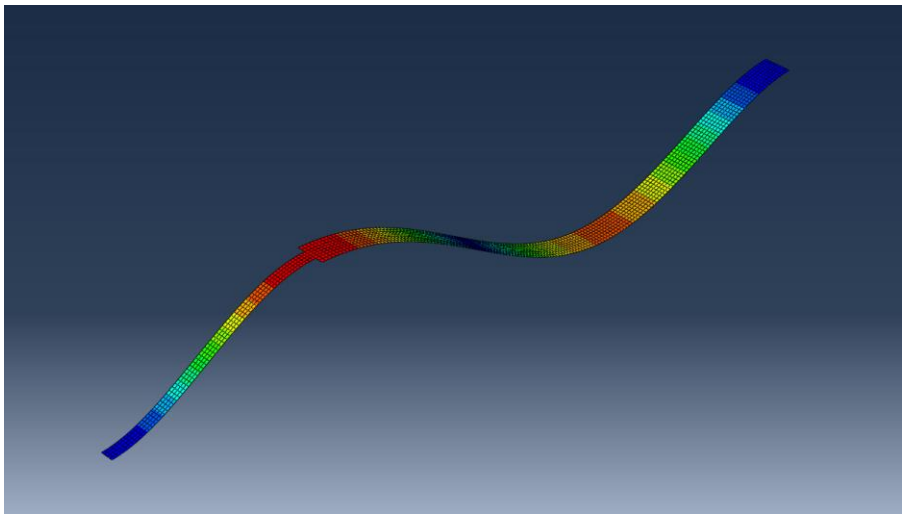

Figure 7: Mode 2 Shape

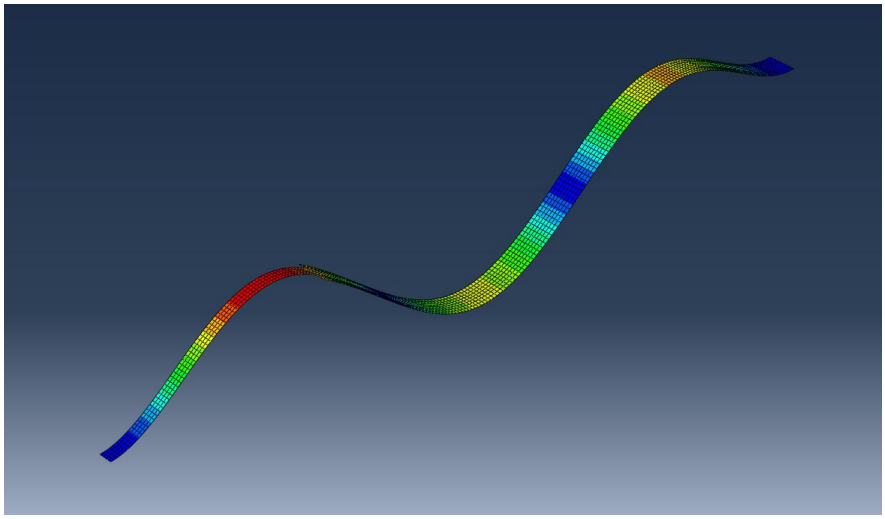

Figure 8: Mode 3 Shape

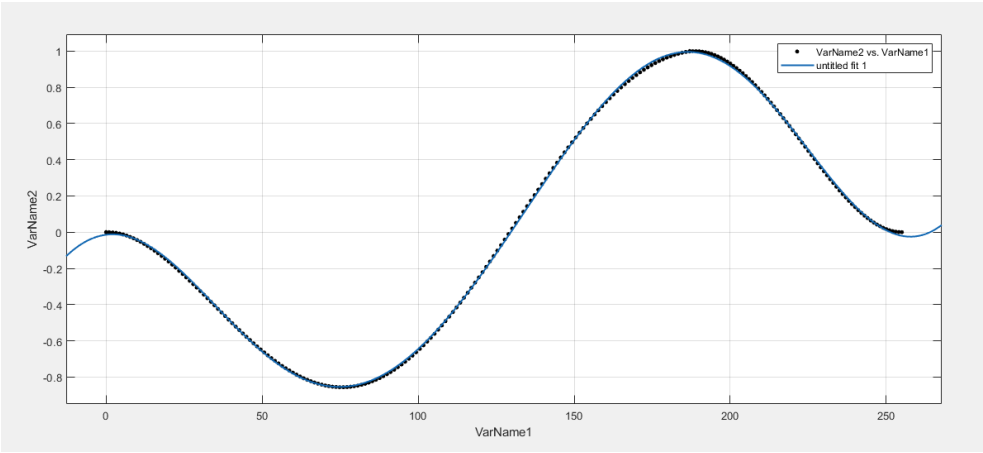

Figure 9: Mode 2 XY-Data

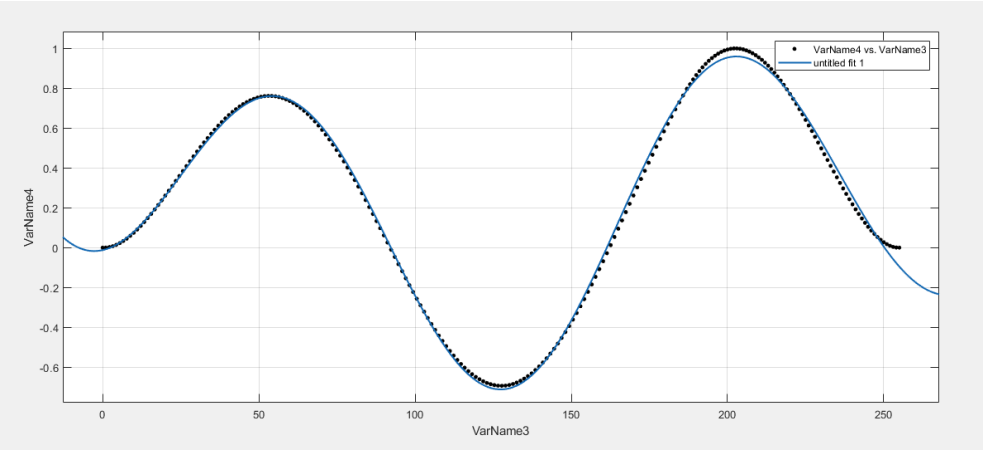

Figure 10: Mode 3 XY-Data

General model Sin3:
f(x) =
a1*sin(b1*x+c1) + a2*sin(b2*x+c2) + a3*sin(b3*x+c3)
Coefficients (with 95% confidence bounds):
a1 = 1.098 (-0.626, 2.822)
b1 = 0.006104 (-0.004952, 0.01716)
c1 = 5.525 (4.152, 6.897)
a2 = 0.9542 (-0.0003983, 1.909)
b2 = 0.03976 (0.03673, 0.04279)
c2 = 1.143 (0.8245, 1.461)
a3 = 0.4118 (-0.4951, 1.319)
b3 = 0.047 (0.0389, 0.05509)
c3 = 3.456 (2.487, 4.425)

Goodness of fit:
SSE: 0.0147
R-square: 0.9998
Adjusted R-square: 0.9998
RMSE: 0.008155

Figure 11: Mode 2 Generated Equation

General model Sin3:
f(x) =
a1*sin(b1*x+c1) + a2*sin(b2*x+c2) + a3*sin(b3*x+c3)
Coefficients (with 95% confidence bounds):
a1 = 0.6864 (0.6221, 0.7506)
b1 = 0.04458 (0.04339, 0.04577)
c1 = -1.04 (-1.201, -0.8795)
a2 = 1.981 (-181.6, 185.6)
b2 = 0.005986 (-0.5165, 0.5285)
c2 = 1.889 (-95.73, 99.51)
a3 = 1.502 (-231.3, 234.4)
b3 = 0.01099 (-0.2797, 0.3017)
c3 = 4.19 (-39.89, 48.27)

Goodness of fit:
SSE: 0.1132
R-square: 0.9981
Adjusted R-square: 0.998
RMSE: 0.02263

Figure 12: Mode 3 Generated Equation

2.3 Dynamic Analysis

Analytical fields were created in ABAQUS using the fitted sum of sine equations characterizing the second and third mode obtained in MATLAB. These analytical fields were then applied onto the top surface of the beam as displacement initial conditions shown in Figures 13 and 14. These initial conditions caused the structure to initially deflect at relatively large amplitudes at the corresponding mode shape. The second mode shape was used as an initial condition for the lower mode excitation whereas the third mode shape was used for the higher mode excitation. As an attempt to achieve higher levels of internal resonance, both mode shapes at various magnitudes were combined into a single equation for the initial condition for certain scenarios. The structure was then released to freely oscillate until the response reached steady state. The calculated damping coefficient was implemented beforehand so that the structure would experience a free decay response where energy of the system was dissipated and the oscillation amplitude approached zero over time.

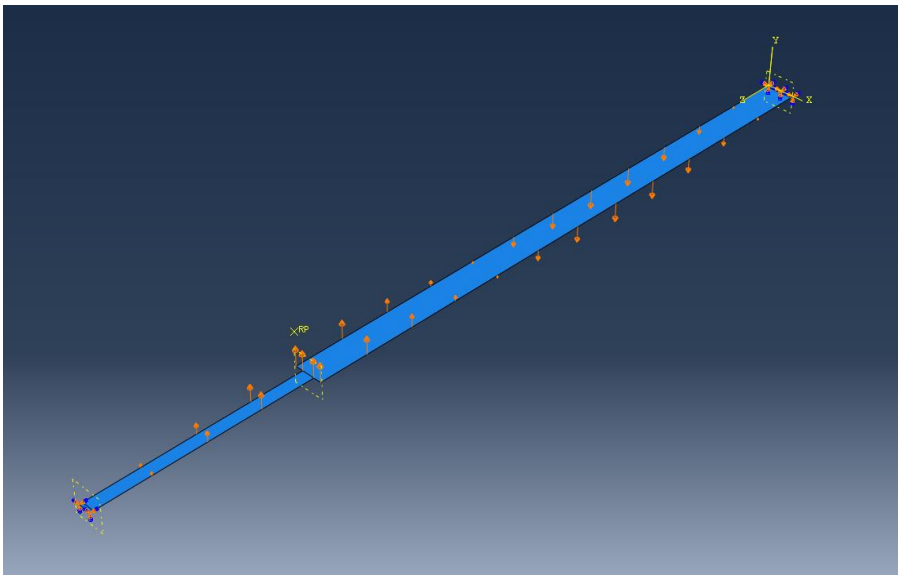

Figure 13: Mode 2 Initial Condition

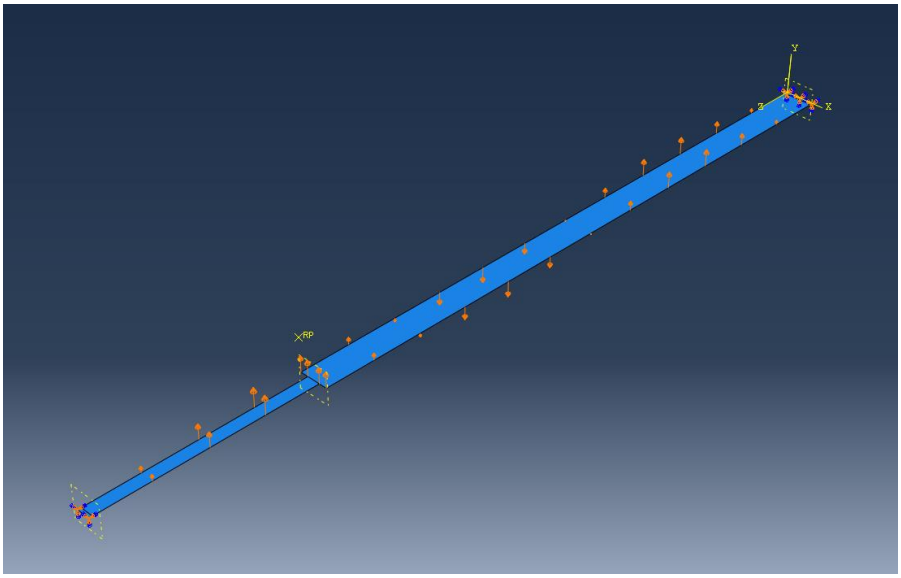

Figure 14: Mode 3 Initial Condition

2.3 Post Processing

Once the dynamic simulation was completed, the displacement data along the y-axis of the free decay response was extracted at multiple locations of the structure and imported into Excel. These locations include the points of maximum amplitude and nodes (where zero amplitude occurs) for both the second and third mode shapes. The displacement data was then plotted using MATLAB generating the time response of the system which shows amplitude with respect to time. FFT was then performed on the data to obtain the frequency response of the system. This plot shows amplitude with respect to frequency which helps identify the mode shapes being engaged. WT was also performed to show the frequency content and intensity at any given time of the simulation. This plot helps identify the presence of modal frequencies at different time intervals which is very useful for detecting intermodal energy transfer. The MATLAB code generating the frequency response and wavelet transform plots are shown in the Appendix in Figure 15.

Chapter 3: Results

3.1 Preprocessing Results

By conducting a linear perturbation analysis on the model through ABAQUS, the first three mode shapes and their corresponding natural frequencies were obtained. Shown in Table 2 are the frequencies for the first three mode shapes. Note that the Young's Modulus was changed until the second mode shape frequency was approximately half of the third mode shape frequency in order to achieve a 1:2 ratio. Using the first two mode shape frequencies and converting them to rad/s, the damping coefficient was calculated to be 357.757 Ns/m. This value was implemented into the material properties so that the system experienced a free decay response during the dynamic analysis where the amplitude gradually approached zero over time. Table 3 shows the fitted equations defining the second and third mode shapes which were obtained from MATLAB's curve fitting tool.

Table 2: Modal Frequencies

Mode Shape	Frequency (kHz)
1	35.017
2	152.669
3	310.020

Table 3: Mode Shape Equations

Mode Shape	Fitted Equation
2	$f_2 = 1.098\sin(0.006104x + 5.525) + 0.9542\sin(0.03976x + 1.143) + 0.4118\sin(0.047x + 3.456)$
3	$f_3 = 0.6864\sin(0.04458x - 1.04) + 1.981\sin(0.005986x + 1.889) + 1.502\sin(0.01099x + 4.19)$

Five different cases were tested for the dynamic analysis with each one differing in the initial condition used. The first scenario was the lower mode excitation where the beam was initially deflected at the second mode shape. The second scenario was the higher mode excitation where beam was initially deflected at the third mode shape. The third scenario was the dominant excitation of the lower mode which involved exciting both mode shapes where the second mode was deflected at a displacement ten times larger than the third mode. The fourth scenario was the dominant excitation of the higher mode where the third mode was deflected at a displacement ten times larger than the second mode. The last scenario was the combined mode excitation which involved both mode shapes being deflected at the same magnitude. Table 4 shows the initial conditions used for each scenario and their corresponding equations that were employed onto the top surface of the structure. All dynamic simulations ran for over 12,000 μs and different sets of displacement data were taken at the points of maximum amplitude and nodes for both the second and third mode shapes. By plotting this data through MATLAB the time responses were obtained.

Table 4: Initial Conditions for Dynamic Analysis

Description	Initial Condition	Equation
Lower Mode Excitation	Mode 2 shape at 0.40 μm	$0.40f_2$
Higher Mode Excitation	Mode 3 shape at 0.40 μm	$0.40f_3$
Dominant Excitation of Lower Mode	Mode 2 shape at 0.40 μm Mode 3 shape at 0.04 μm	$0.40f_2 + 0.04f_3$
Dominant Excitation of Higher Mode	Mode 2 shape at 0.04 μm Mode 3 shape at 0.40 μm	$0.04f_2 + 0.40f_3$
Combined Mode Excitation	Mode 2 shape at 0.40 μm Mode 3 shape at 0.40 μm	$0.40f_2 + 0.40f_3$

3.2 Lower Mode Excitation

For the lower mode excitation, the beam was initially deformed using the second mode shape with a maximum amplitude of 0.40 μm. The time responses at all points of interest are shown in Table 5. The FFT plots in Table 6 show large peaks in amplitude at the second mode frequency. The third mode appears to be slightly engaged since there are small peaks in amplitude at its respective frequency. The WT plots in Table 7 show the frequency content of the system throughout different points in time where the darkness of an area corresponds to amplitude size. The second mode shape was forcefully engaged which is shown by the lines starting near 200 kHz which converge at approximately 150 kHz. The slight engagement of the third mode shape is shown by the lines starting near 350 kHz which converge at approximately 310 kHz. The second mode frequency is most active at the locations of the mode 2 and 3 maximum amplitudes. Slight activity of the third mode is found at these locations as well. At the mode 2 node there is very little activity of both the second and third mode frequencies. At the mode 3 node only the second mode frequency is significantly active. Since a relatively large deflection was exhibited, the system was subject to a large force which caused it to experience a slight hardening effect where the engaged modal frequencies were initially detuned to higher values. As the system approached steady state these frequencies decreased to their appropriate values which is why the lines in the WT plot appear to be initially curved. The large forcing also caused the system to exhibit minor noise levels which is why other undesirable frequencies were experienced.

Table 5: Time Response of Lower Mode Excitation

Mode 2 Max Amplitude	Mode 2 Node
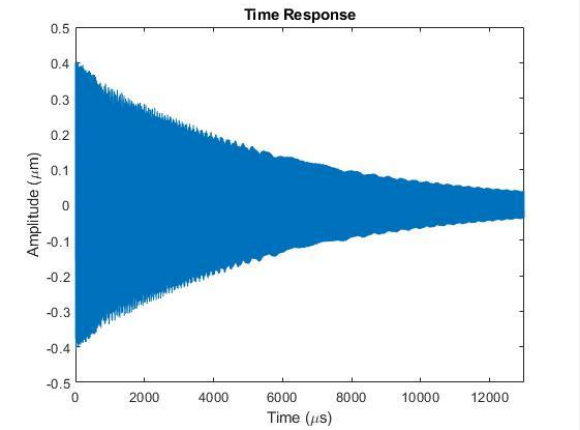	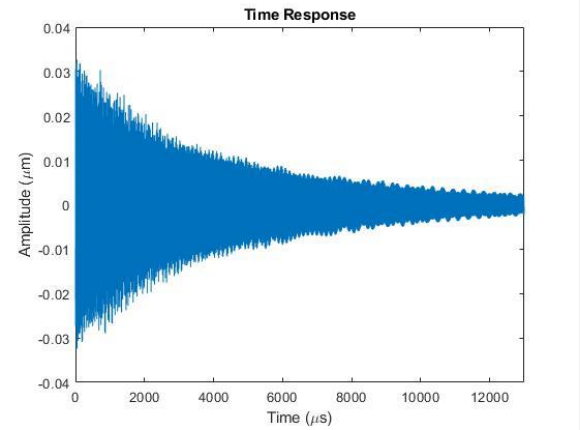
Mode 3 Max Amplitude	**Mode 3 Node**
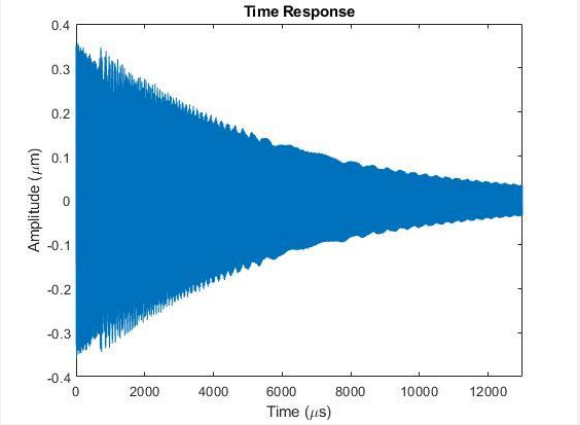	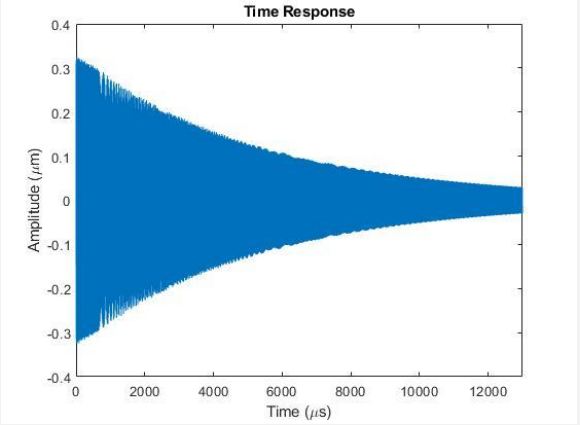

Table 6: FFT of Lower Mode Excitation

Mode 2 Max Amplitude	Mode 2 Node
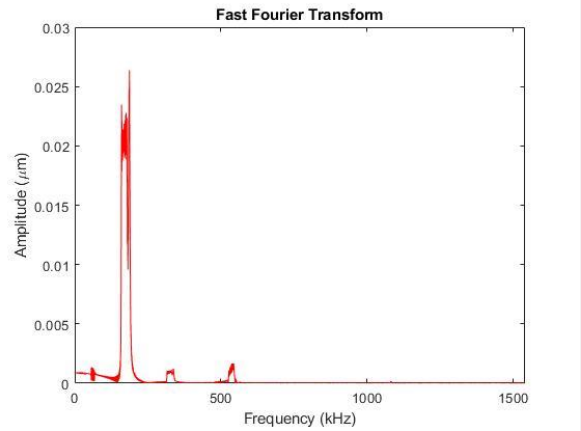	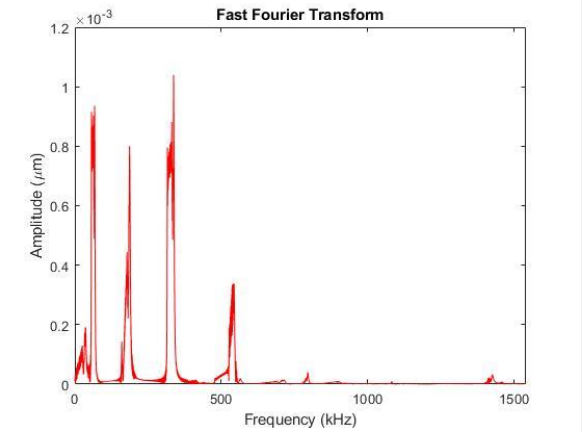
Mode 3 Max Amplitude	**Mode 3 Node**
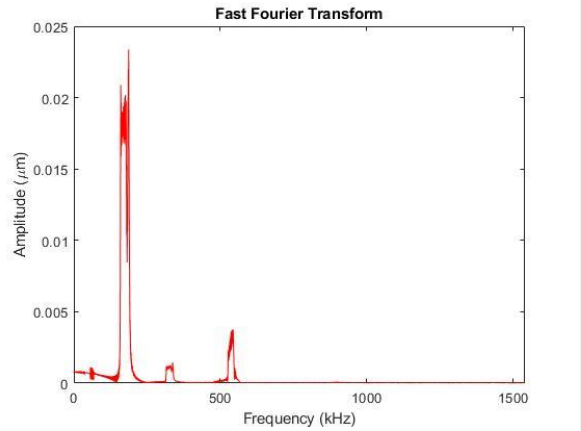	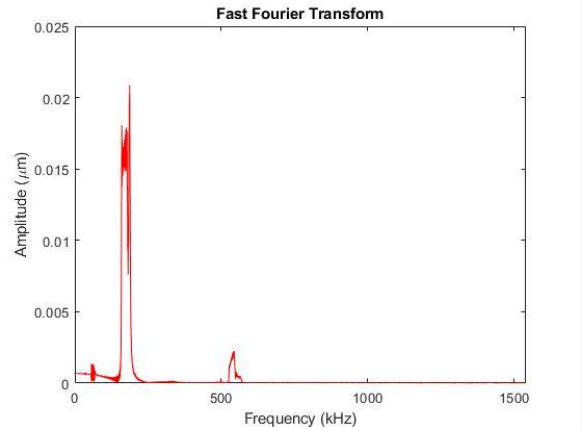

Table 7: WT of Lower Mode Excitation

Mode 2 Max Amplitude	Mode 2 Node
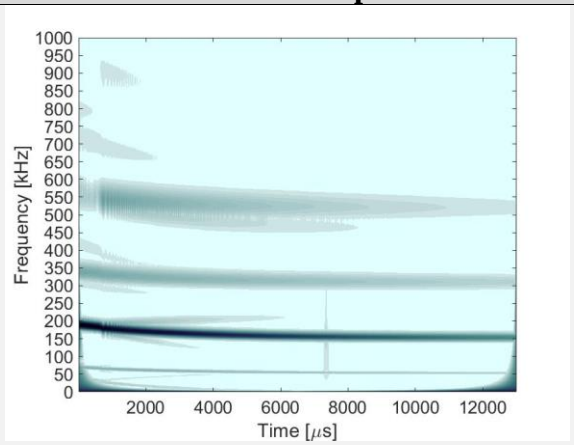	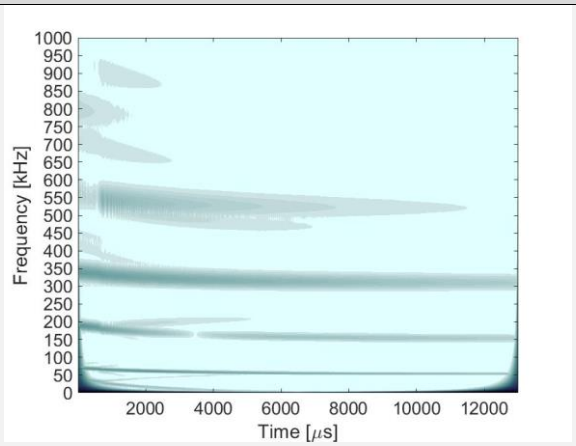
Mode 3 Max Amplitude	**Mode 3 Node**
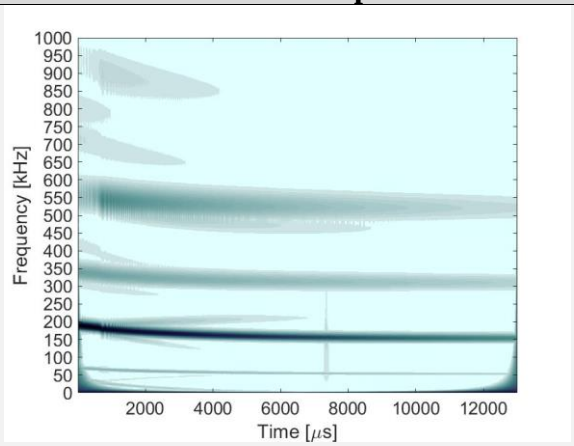	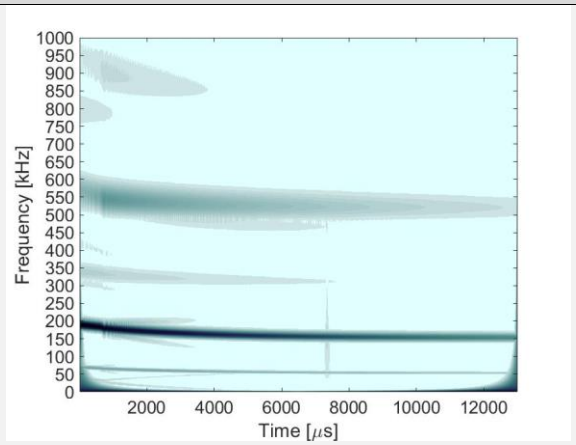

3.3 Higher Mode Excitation

For the higher mode excitation, the beam was initially deformed using the third mode shape with a maximum amplitude of 0.40 μm. The time responses are shown in Table 8. The FFT plots in Table 9 show large peaks in amplitude at the third mode frequency and small peaks at the second mode frequency. The WT plots in Table 10 show the third mode shape being primarily engaged which corresponds to the lines starting near 400 kHz which converge at approximately 310 kHz. The slight engagement of the second mode shape is shown by the lines starting near 200 kHz which converge at approximately 150 kHz. The third mode frequency is most active at the locations of the mode 2 and 3 maximum amplitudes. The second mode frequency is slightly active at these locations as well. At the mode 2 node only the third mode frequency is significantly active. At the mode 3 node there is very little activity of both the second and third mode frequencies. This simulation experienced similar noise levels as the lower mode excitation but exhibited a more significant hardening effect.

Table 8: Time Response of Higher Mode Excitation

Mode 2 Max Amplitude	Mode 2 Node
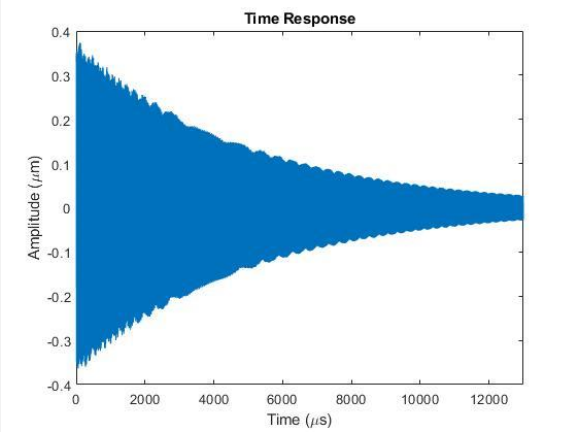	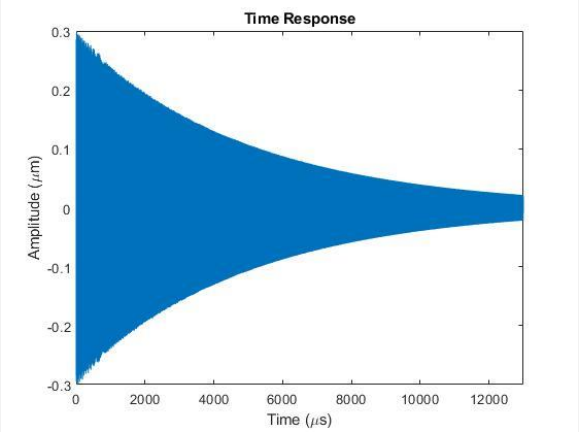
Mode 3 Max Amplitude	**Mode 3 Node**
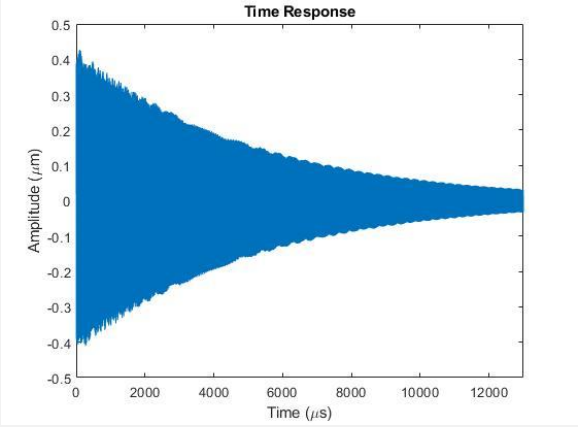	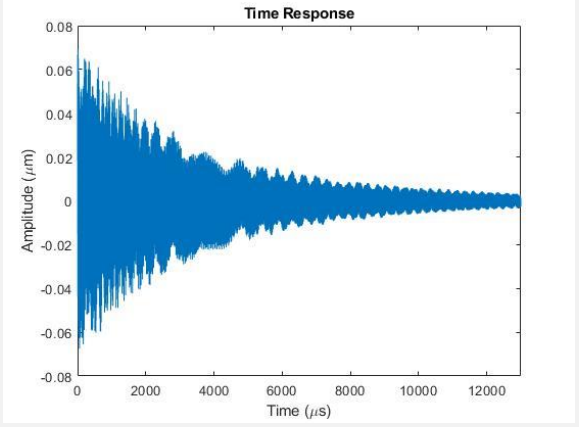

Table 9: FFT of Higher Mode Excitation

Mode 2 Max Amplitude	Mode 2 Node
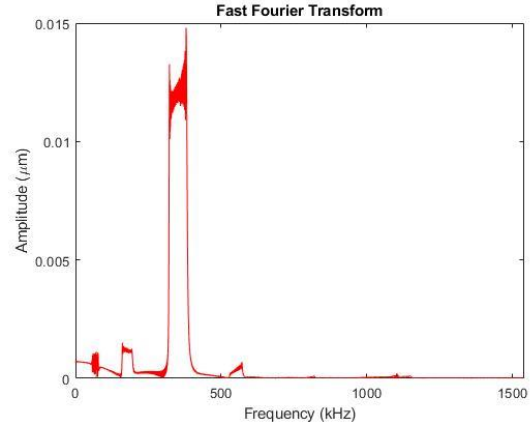	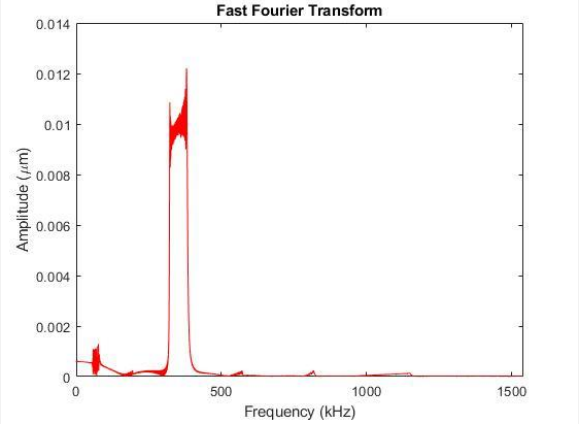
Mode 3 Max Amplitude	**Mode 3 Node**
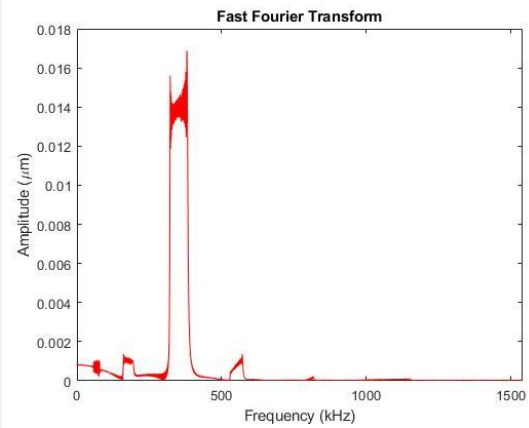	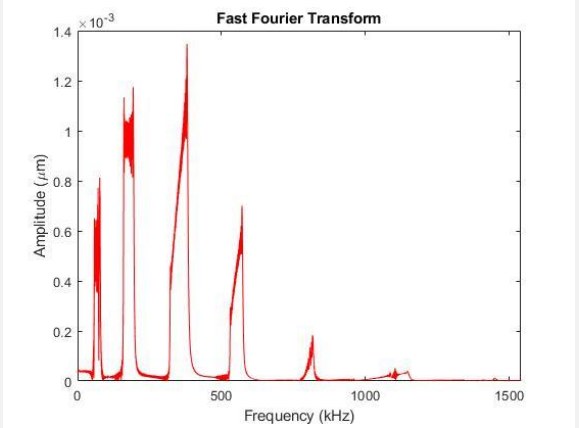

Table 10: WT of Higher Mode Excitation

Mode 2 Max Amplitude	Mode 2 Node
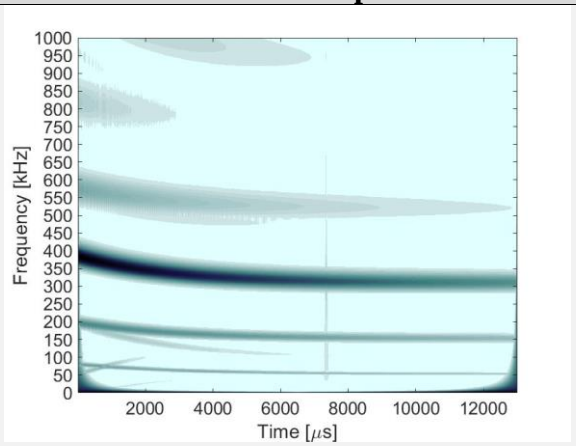	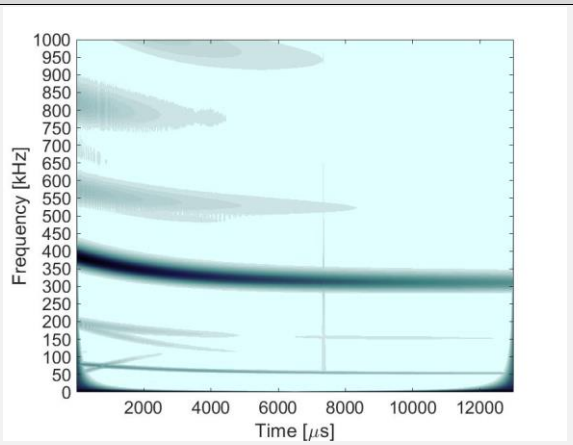
Mode 3 Max Amplitude	**Mode 3 Node**
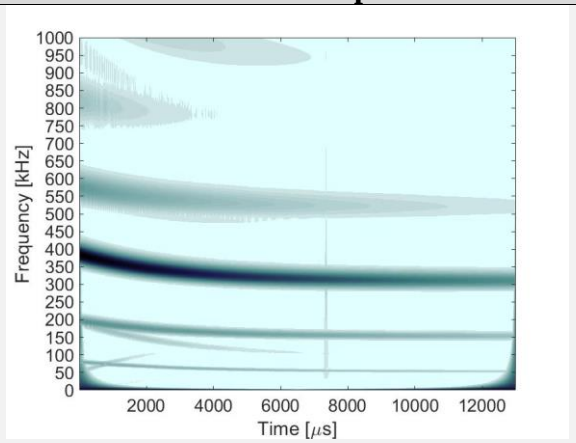	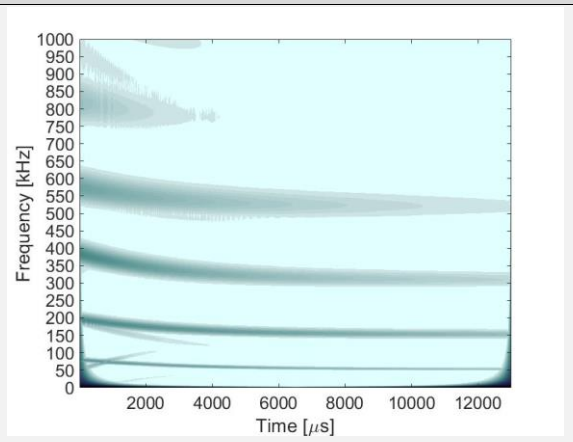

3.4 Dominant Excitation of Lower Mode

For the dominant excitation of the lower mode, the beam was initially deformed at the second and third mode shapes with maximum amplitudes of 0.40 μm and 0.04 μm respectively. The time responses are shown in Table 11. The FFT plots in Table 12 show large levels of amplitude at the second mode frequency and small levels of amplitude at the third mode frequency. The WT plots in Table 13 show the second mode frequency being heavily engaged which corresponds to the lines starting near 200 kHz which converge at approximately 150 kHz. The slight engagement of the third mode shape is shown by the lines starting near 350 kHz which converge at approximately 310 kHz. Both modal frequencies are most active at the locations of the mode 2 and 3 maximum amplitudes. At the mode 2 node there is very little activity of these modal frequencies. At the mode 3 node only the second mode frequency is significantly active. This simulation experienced a hardening effect and excessive noise as well due to the large amount of forcing. This simulation produced similar results to the lower mode excitation. The main difference between them is that the third mode frequency exhibited slightly higher amplitudes in this simulation since it was externally excited at a small degree.

Table 11: Time Response of Dominant Excitation of Lower Mode

Mode 2 Max Amplitude	Mode 2 Node
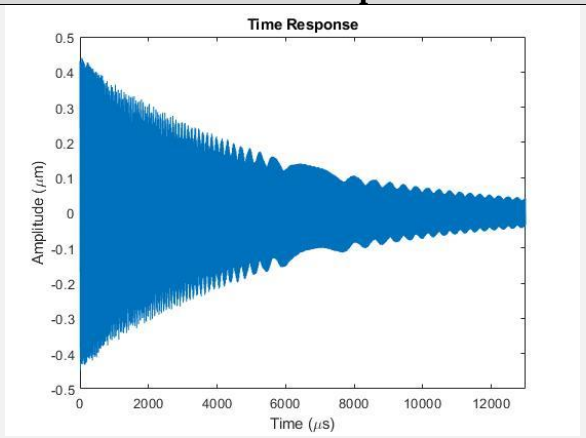	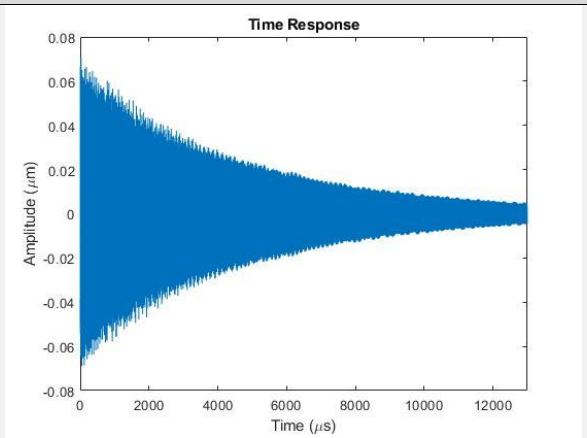
Mode 3 Max Amplitude	**Mode 3 Node**
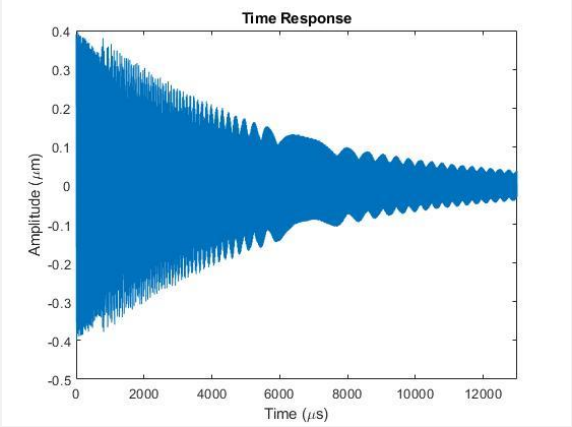	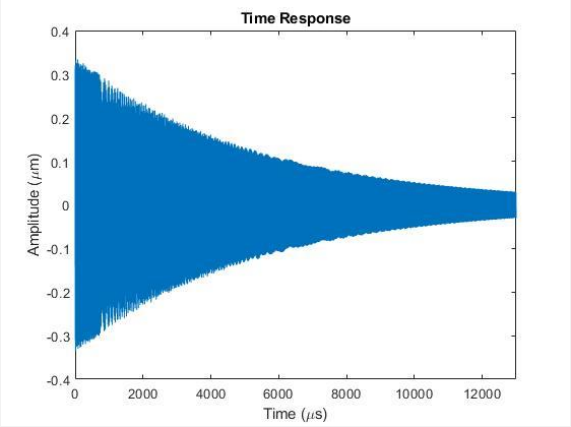

Table 12: FFT of Dominant Excitation of Lower Mode

Mode 2 Max Amplitude	Mode 2 Node
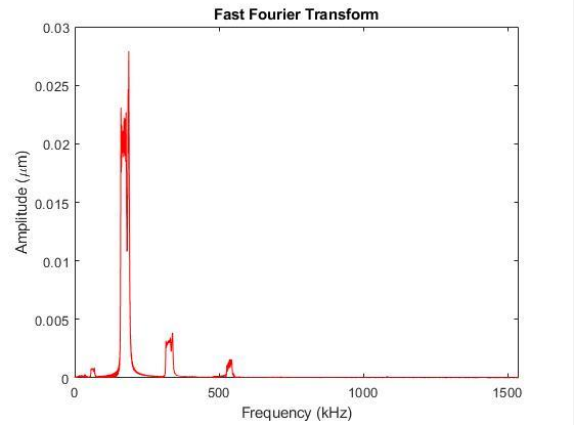	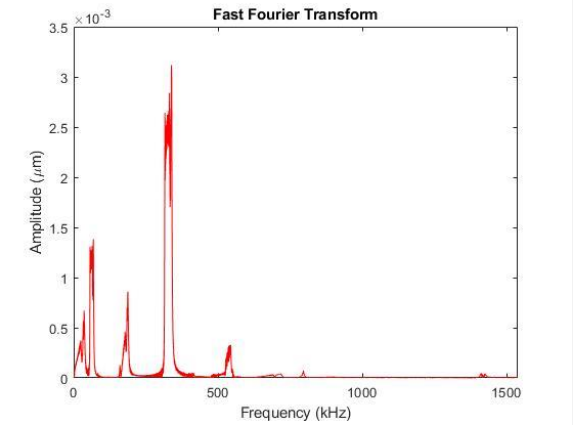
Mode 3 Max Amplitude	**Mode 3 Node**
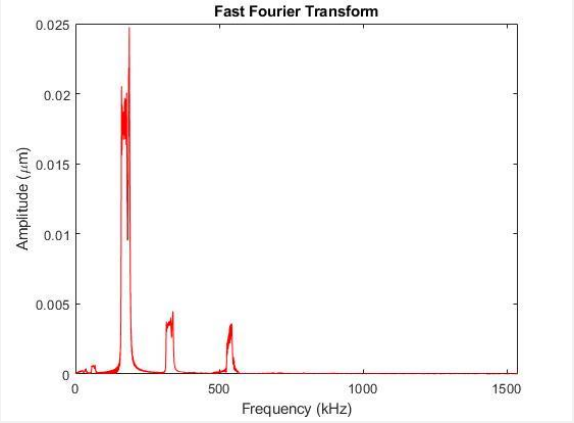	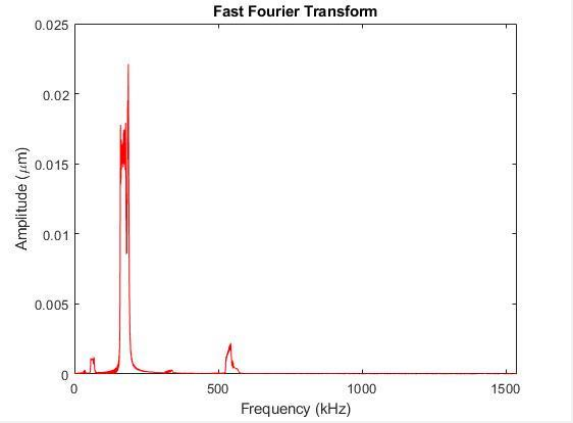

Table 13: WT of Dominant Excitation of Lower Mode

Mode 2 Max Amplitude	Mode 2 Node
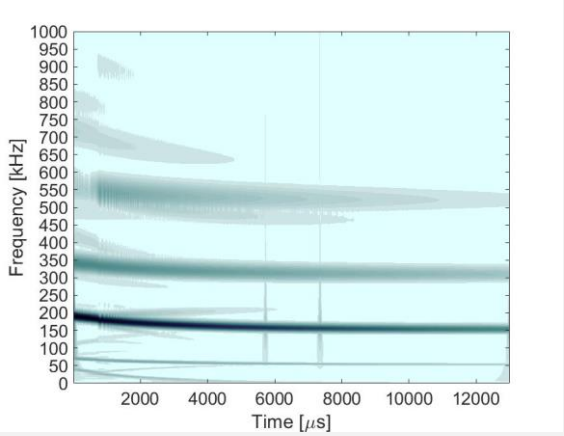	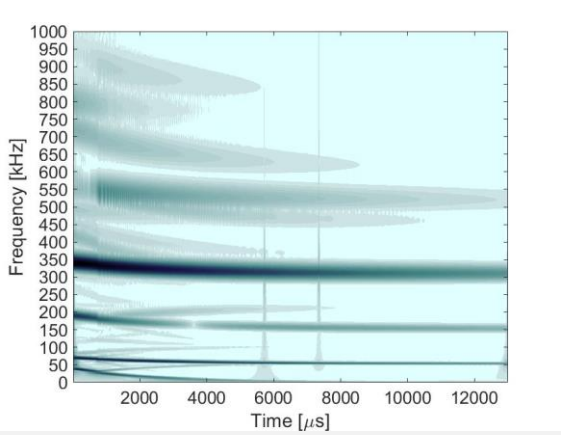
Mode 3 Max Amplitude	**Mode 3 Node**
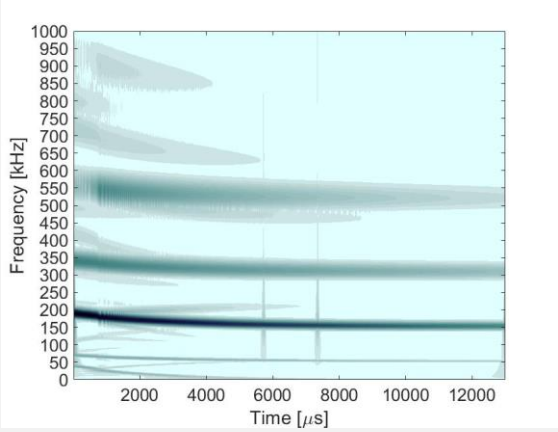	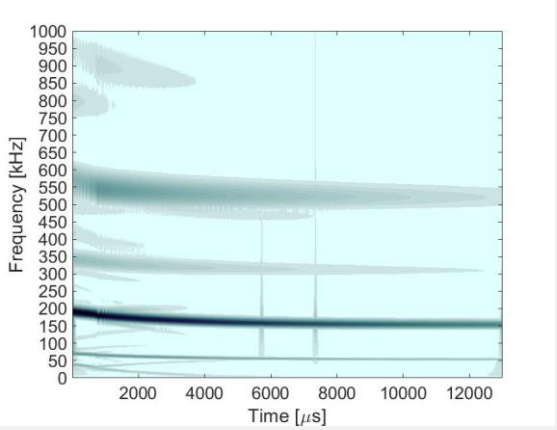

3.5 Dominant Excitation of Higher Mode

For the dominant excitation of the higher mode, the beam was initially deformed at the second and third mode shapes with maximum amplitudes of 0.04 μm and 0.40 μm respectively. The time responses are shown in Table 14. The FFT plots in Table 15 show large levels of amplitude at the third mode frequency and small levels of amplitude at the second mode frequency. The WT plots in Table 16 show the third mode frequency being heavily engaged which corresponds to the lines starting near 400 kHz which converge at approximately 310 kHz. The slight engagement of the second mode shape is shown by the lines starting near 200 kHz which converge at approximately 150 kHz. Both modal frequencies are most active at the locations of the mode 2 and 3 maximum amplitudes. At the mode 2 node only the second mode frequency is significantly active. At the mode 3 node there is very little activity of both modal frequencies. This simulation experienced similar noise levels as the dominant excitation of the lower mode but exhibited a more significant hardening effect. This simulation produced very similar results to the higher mode excitation.

Table 14: Time Response of Dominant Excitation of Higher Mode

Mode 2 Max Amplitude	Mode 2 Node
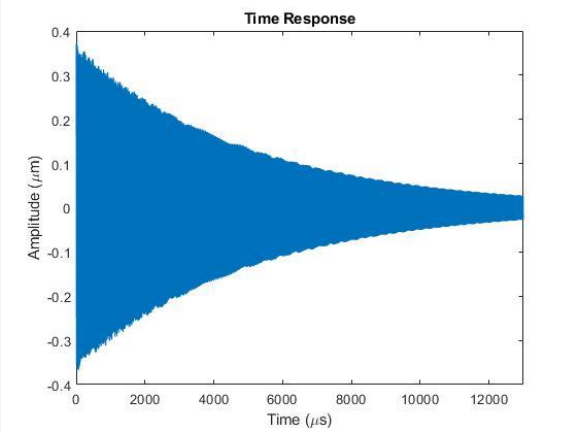	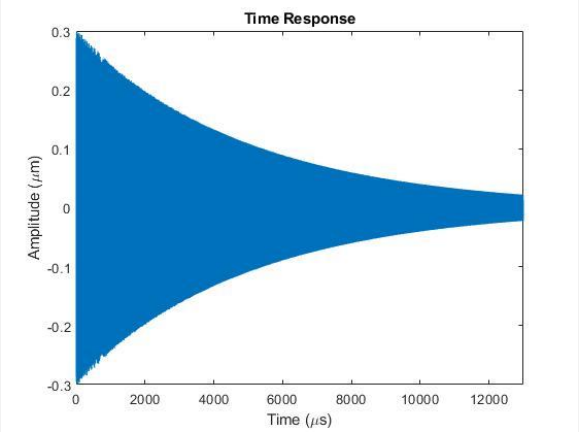
Mode 3 Max Amplitude	**Mode 3 Node**
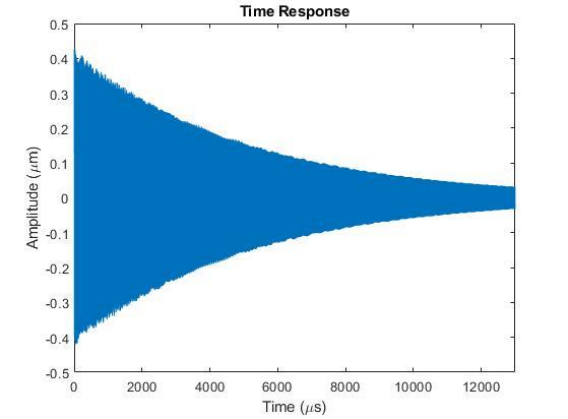	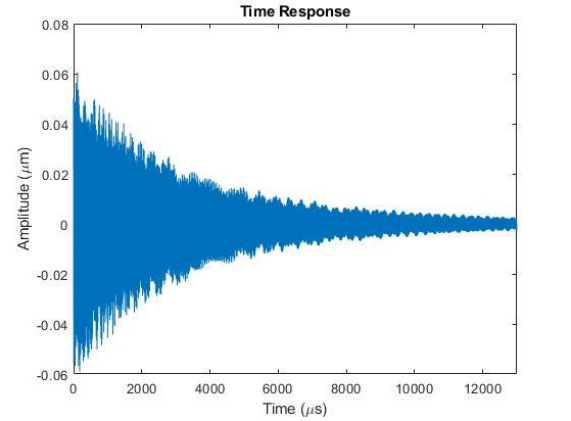

Table 15: FFT of Dominant Excitation of Higher Mode

Mode 2 Max Amplitude	Mode 2 Node
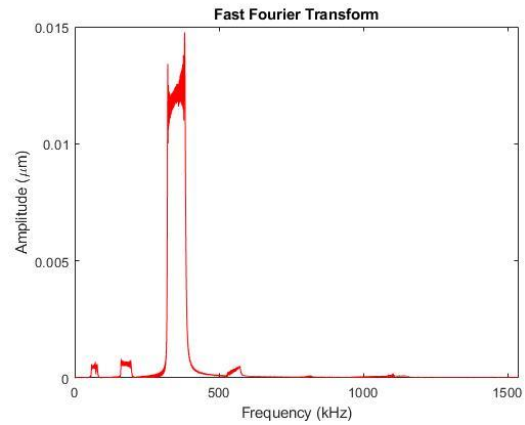	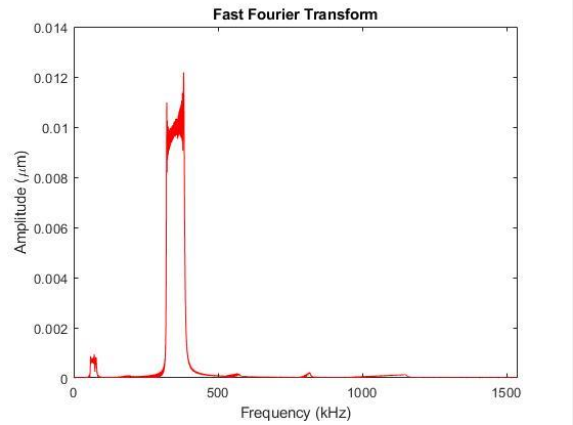
Mode 3 Max Amplitude	**Mode 3 Node**
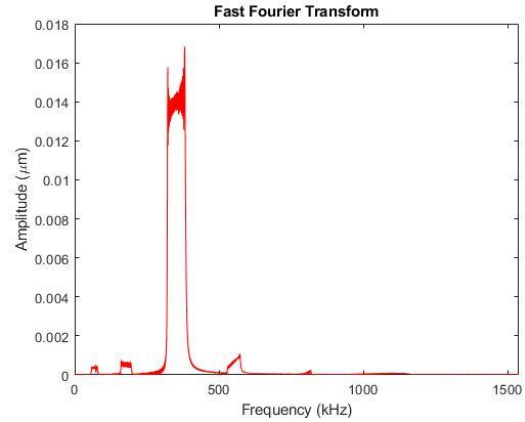	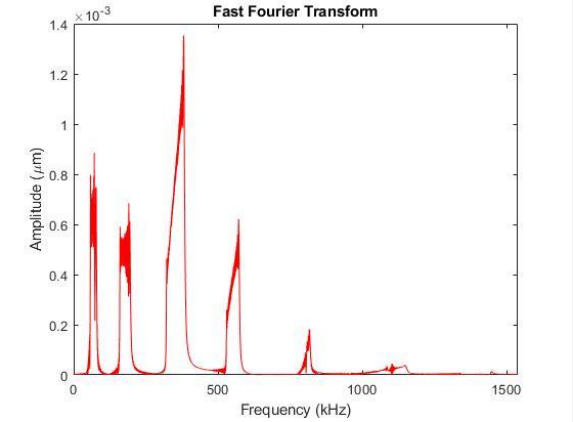

Table 16: WT of Dominant Excitation of Higher Mode

Mode 2 Max Amplitude	Mode 2 Node
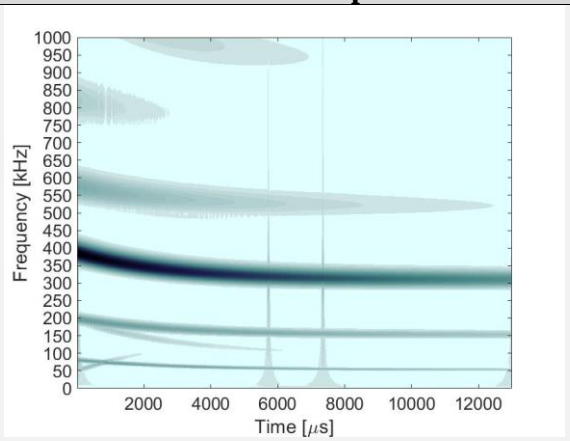	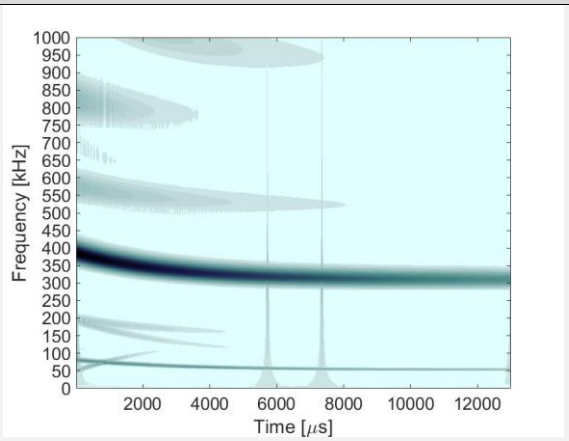
Mode 3 Max Amplitude	**Mode 3 Node**
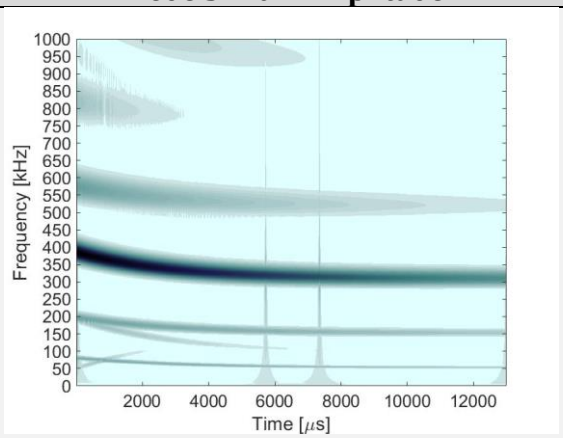	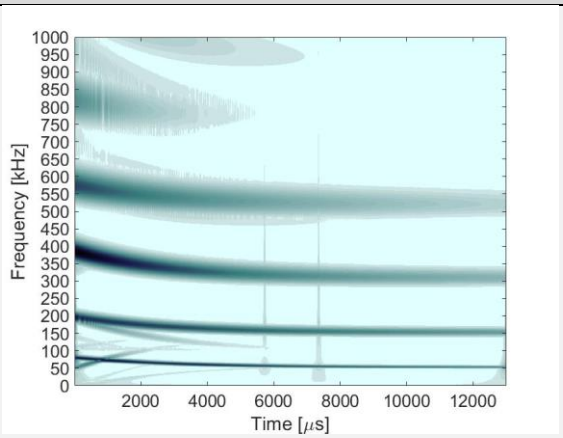

3.6 Combined Mode Excitation

The combined mode excitation involved initially deforming the beam at both the second and third mode shapes with maximum amplitudes of 0.40 μm. The time responses are shown in Table 17. The FFT and WT plots are shown in Tables 18 and 19 respectively. The FFT plots show large levels of amplitude at both the second and third mode frequencies. The WT plots show that both modal frequencies were heavily engaged throughout the entire simulation. The second mode frequency is represented by the lines starting near 250 kHz which converge at approximately 150 kHz. The third mode frequency is represented by the lines starting near 450 kHz which converge at approximately 310 kHz. Both modal frequencies exhibit large amplitudes at the locations of the mode 2 and 3 maximum amplitudes. At the mode 2 node only the third mode frequency is significantly active. At the mode 3 node only the second mode frequency is significant. This simulation exhibited the strongest hardening effect and noise levels compared to the other simulations since the total forcing level was the greatest.

Table 17: Time Response of Combined Mode Excitation

Mode 2 Max Amplitude	Mode 2 Node
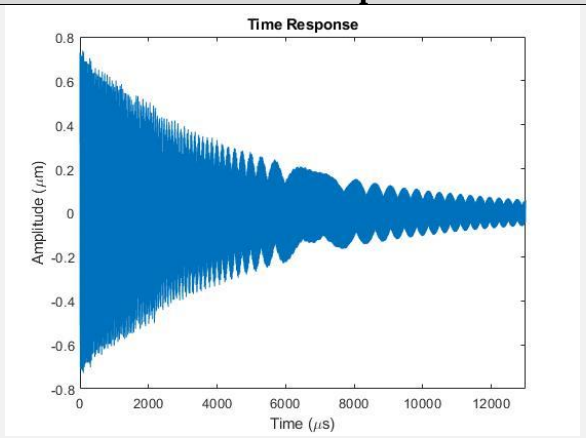	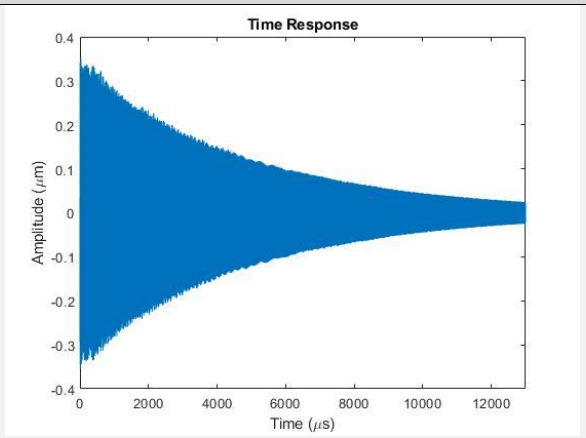
Mode 3 Max Amplitude	**Mode 3 Node**
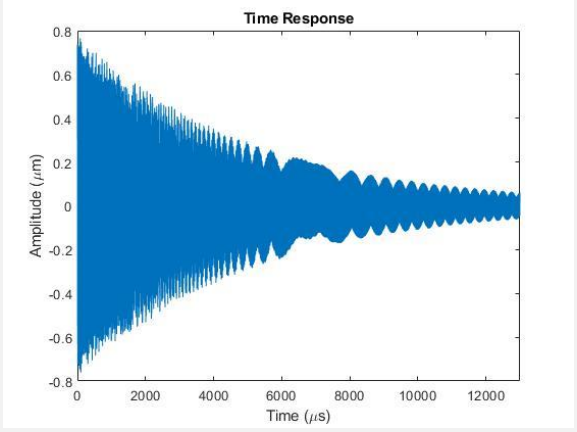	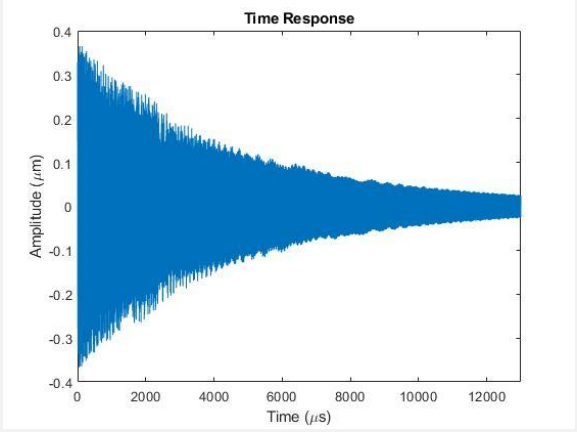

Table 18: FFT of Combined Mode Excitation

Mode 2 Max Amplitude	Mode 2 Node
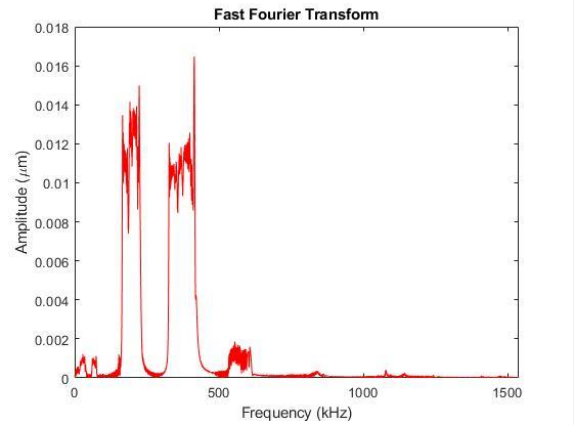	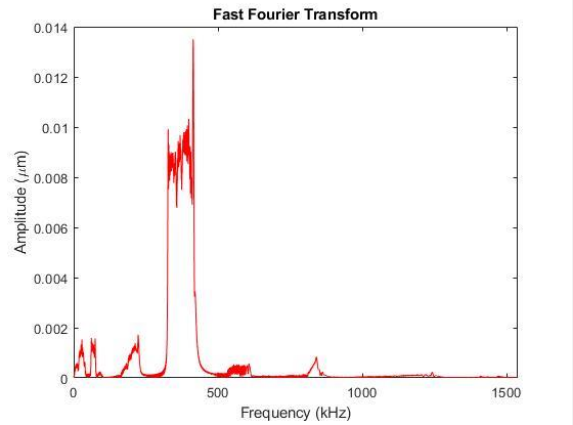
Mode 3 Max Amplitude	**Mode 3 Node**
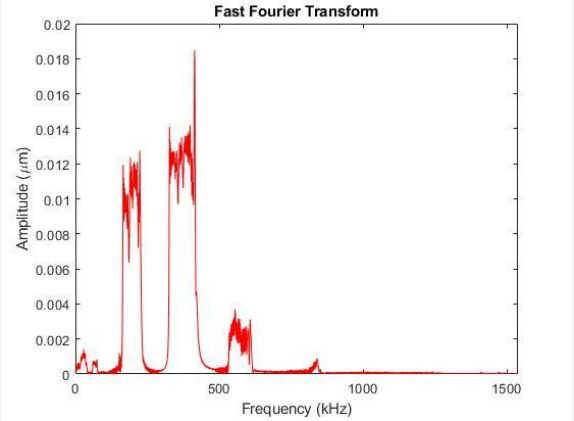	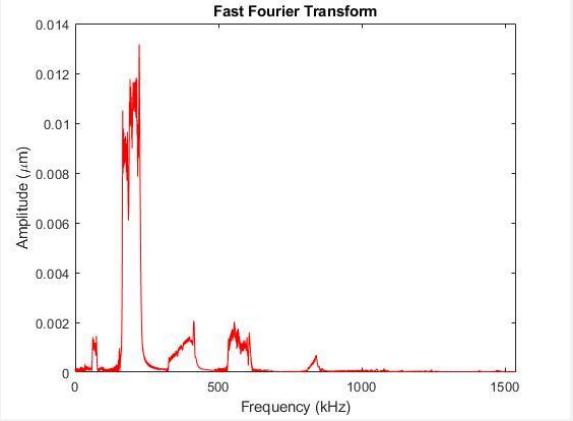

Table 19: WT of Combined Mode Excitation

Mode 2 Max Amplitude	Mode 2 Node
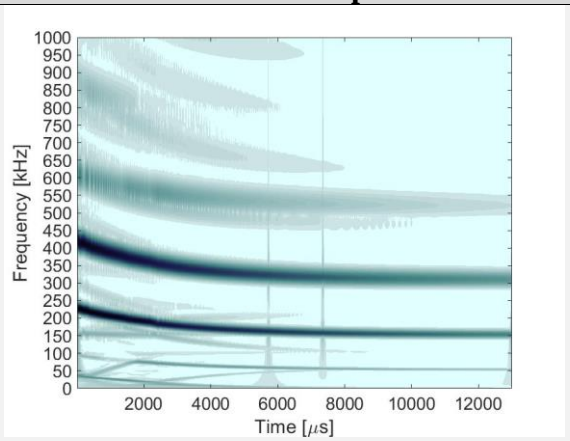	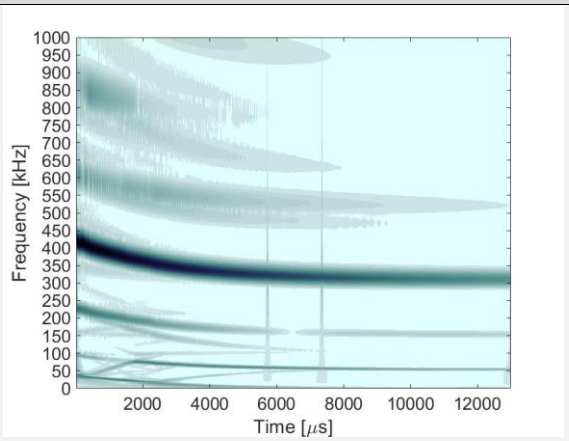
Mode 3 Max Amplitude	**Mode 3 Node**
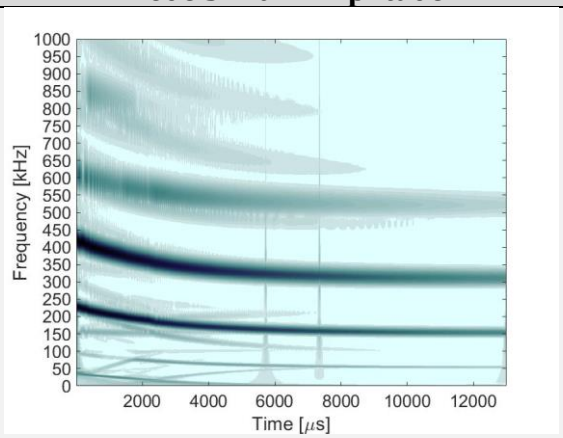	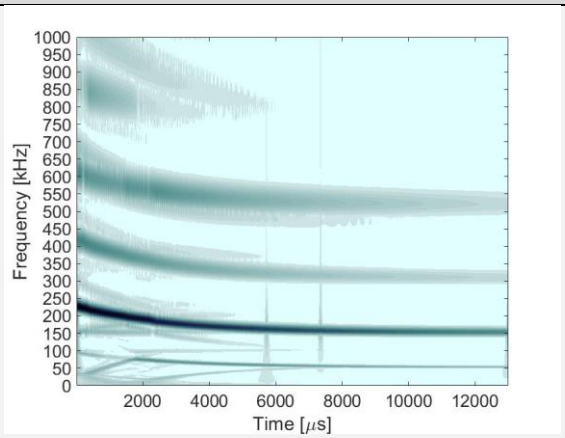

3.7 Discussion of Results

The magnitudes of displacement used for initial conditions were determined through a series of simulations. By comparing the results from one another, the value of 0.40 μm was estimated to produce enough force to cause the system to become nonlinear while also mitigating noise levels as much as possible. Values significantly higher than 0.40 μm generally produced undesirable amounts of noise while values significantly lower caused the system to exhibit a linear response. We attempted to trigger internal resonance by altering the levels of displacement which would ultimately change the force, but all results came out negative. Even after successfully establishing a 1:2 ratio between the second and third mode frequencies and ensuring nonlinear behavior, internal resonance was still not realized. Based off the FFT and WT data for the lower and higher mode excitations, the internally resonated modes were indirectly engaged at very small magnitudes, however, no prominent energy transfer between the coupled modes was experienced. If intermodal energy transfer was successfully triggered, then the externally resonated mode would have experienced a decrease in amplitude while the internally resonated mode would have exhibited an increase in amplitude. For the WT plots of the lower mode excitation, there should be dark lines corresponding to the second mode frequency that gradually fade out while the lines corresponding to the third mode frequency should start off light and then gradually darken over time. The WT plots of the higher mode excitation should experience the opposite where the dark lines corresponding to the third mode frequency fade out while the lines corresponding to the second mode frequency gradually darken.

The simulations for the dominant excitation of the lower and higher modes were performed since the results for the lower and higher mode excitations did not show any signs of internal resonance. For these simulations we gave a slight excitation to the internally resonated mode

through the initial conditions to see if it had any effect on internal resonance. The results produced ended up being similar to the ones from our initial simulations. The combined mode excitation was performed afterwards to see if the system would exhibit any form of intermodal energy transfer when both mode shapes were heavily engaged. This last scenario ended up producing negative results as well. All five scenarios exhibited a hardening affect which was caused by an increased stiffness in the beam when a large force was exerted. Noise was also experienced at varying degrees for each simulation which was also a result of the large forcing.

Chapter 4: Conclusion

4.1 Summary

The overall results of this research came out negative and internal resonance was not effectively triggered. In this research we attempted to couple the second and third mode shapes for our beam design. For the modal analysis we were successful in creating a 1:2 ratio between the second and third mode shapes while designating a Young's Modulus value within a reasonable range of silicon. Initial conditions used for the dynamic analysis included deflecting the beam at the corresponding mode shapes. The lower mode excitation used the second mode shape to excite the system while the higher mode excitation used the third mode shape. The results produced by these simulations did not show anything significant, so we attempted to trigger internal resonance by combining the mode shapes at various magnitudes. The dominant excitation of the lower mode involved a primary excitation of the second mode while also exciting the third mode at a much smaller magnitude. The dominant excitation of the higher mode involved a primary excitation of the third mode while also exciting the second mode at a smaller magnitude. These simulations rendered similar results, so the combined mode excitation was performed to see if the system would exhibit any energy transfer if both mode shapes were simultaneously excited at large magnitudes. Based off the dynamic data for all cases, both the second and third modes were properly engaged, however, after investigating the WT plots, no prominent energy transfer between the two modes was found.

4.2 Future Work

Additional parameters will need to be investigated if internal resonance were to be effectively triggered. The amount of displacement applied to the initial conditions was the main parameter investigated throughout this research. When the beam was initially displaced at higher

magnitudes, the structure would exhibit increased levels of forcing. Many simulations were performed at different amounts of forcing to investigate its influence on the dynamic behavior of the system. A large amount of force is required to trigger internal resonance, but by increasing this, the system only experienced increased levels of nonlinearity and noise. Intermodal energy transfer was never evident no matter what forcing levels were used. Other parameters will have to be investigated in order to obtain the design criteria to effectively realize internal resonance. Parameters as such include the type of initial condition used or the material and geometric properties of the beam design. Ways to mitigate nonlinear hardening and noise levels will also have to be investigated in order to achieve optimal functionality of the system.

References

1. Ozevin, D., 2014. Micro-electro Mechanical Systems. *Sensor Technologies for Civil Infrastructures*. https://www.sciencedirect.com/topics/chemistry/micro-electro-mechanical-systems
2. An Introduction to MEMS. *Loughborough University*, PRIME Faraday Partnership, 2002. http://www.lboro.ac.uk/microsites/mechman/research/ipm-ktn/pdf/Technology_review/an-introduction-to-mems.pdf
3. Mangussi F, Zanette DH (2016) Internal Resonance in a Vibrating Beam: A Zoo of Nonlinear Resonance Peaks. PLoS ONE 11(9): e0162365.
4. Antonio D. *et al*. Frequency stabilization in nonlinear micromechanical oscillators. *Nat. Commun.* 3:806 doi: 10.1038/ncomms1813 (2012).
5. Gusev, Vitalyi & TOURNAT, Vincent. (2005). Amplitude- and frequency-dependent nonlinearities in the presence of thermally-induced transitions in the Preisach model of acoustic hysteresis. Phys. Rev. B. 72. 10.1103/PhysRevB.72.054104.
6. B. Abdo, E. Arbel-Segev, O. Shtempluck and E. Buks, "Observation of Bifurcations and Hysteresis in Nonlinear NbN Superconducting Microwave Resonators," in IEEE Transactions on Applied Superconductivity, vol. 16, no. 4, pp. 1976-1987, Dec. 2006.
7. Karabalin, R & Lifshitz, Ron & Cross, M & Matheny, Matt & Masmanidis, Sotiris & Roukes, Michael. (2011). Signal Amplification by Sensitive Control of Bifurcation Topology. Physical review letters. 106. 094102. 10.1103/PhysRevLett.106.094102.
8. Huang, D., Xu, W., Liu, D., & Han, Q. (2014). Multi-valued responses of a nonlinear vibro-impact system excited by random narrow-band noise. Journal of Vibration and Control, 22(12), 2907–2920.
9. Asadi, K., Li, J., Peshin, S., Yeom, J., Cho, H., 2017. Mechanism of geometric nonlinearity. *Physical Review B*, 96.
10. Asadi K, Yu J, Cho H. 2018 Nonlinear couplings and energy transfers in micro- and nano-mechanical resonators: intermodal coupling, internal resonance and synchronization. *Phil. Trans. R. Soc. A* 376: 20170141.
11. Nayfeh, A. H., & Mook, D. T. (2007). Nonlinear Oscillations. Weinheim: Wiley.
12. Thangavel, G. (2012). Finite Element Analysis of the Direct Drive PMLOM. https://cdn.intechopen.com/pdfs-wm/39760.pdf
13. The Advantages of the Finite Element Method. (2019, August 16). https://innovationatwork.ieee.org/the-advantages-of-fem/
14. Chang, C.-J. (n.d.). Time Frequency Analysis and Wavelet Transform Tutorial. *Time-Frequency Analysis for Biomedical Engineering*, 7–14.
15. Yu, J., Asadi, K., Brahmi, H., & Cho, H. (2019). Tuning Internal Resonance in a MEMS Resonator.

Appendix

```
%% Time Response
clc; clear all; close all;

% Extract Excel data
ss = xlsread('filename.xlsx','A#:A#')-1; % Time (mus)
xx = xlsread('filename.xlsx','B#:B#'); % Amplitude (mum)
tt = (ss)*10^-6; % Converted time (s)

m = (80000);

t = tt(1:m);
x = xx(1:m);
s = ss(1:m);

figure(1)
plot(ss,xx)
title('Time Response')
xlabel('Time (\mus)')
ylabel('Amplitude (\mum)')
xlim([0 max(ss)])

%% Fast Fourier Transform
T = (t(end)-t(1))/length(t); % Sample time
Fs = 1/T;                    % Sampling frequency
L = length(t);
NFFT = 2^nextpow2(L); % Next power of 2 from length of y
Y = fft(x,NFFT)/L;
f = (Fs/2000)*linspace(0,1,NFFT/2+1); % Frequency in kHz

figure(2)
plot(f,2*abs(Y(1:NFFT/2+1)),'r')
title('Fast Fourier Transform')
xlim([0 max(f)/5])
xlabel('Frequency (kHz)')
ylabel('Amplitude (\mum)')

%% Wavelet Transform
n=size(x);
dt=tt(end)/length(tt);
x_part = x(1:500);

% FFT
fs=1/dt;
[p q]= size(t);
T=0:dt:(p-1)*dt;
N=length(x);
y=fft(x,N);

No_Freq = 3000;
IniFreq = 1; FinFreq =1000000; % In Hz
SampleFreq = 1/dt;
F0 = 5;
```

```
[wt.tnew,wt.Freq,wt.Module]=freq_inst_morlet(x,SampleFreq,IniFreq,FinFreq,No_
Freq,F0);
[m,n] = size(wt.Module);
[wt.tnew_twd,wt.Freq_twd,wt.Module_twd]=freq_inst_morlet(x,SampleFreq,IniFreq
,FinFreq,No_Freq,F0);
[m_twd,n_twd] = size(wt.Module_twd);

figure(3)
colormap(pink); MAP=colormap;
colormap(ones(size(MAP))-MAP)
imagesc(wt.tnew*10^6,wt.Freq/10^3,(wt.Module'.^0.4)) % Time in mus and
frequency in kHz
title('Wavelet Transform')
xlabel('Time [\mus]'); ylabel('Frequency [kHz]');
set(gca,'YDir','normal');ylim([0 1000]);
set(gca, 'FontName', 'Arial', 'FontSize', 20)

xlim=([0 4]);
set(gca,'YTick',[0:50:1000]);
x0=10;
y0=10;
width=650;
height=500;
set(gcf,'units','points','position',[x0,y0,width,height])
```

Figure 15: Post Processing MATLAB Code